Agricultural and Forest Meteorology 374 (2025) 110776

Contents lists available at ScienceDirect

Agricultural and Forest Meteorology

journal homepage: www.elsevier.com/locate/agrformet

Enhancing carbon flux estimation in a crop growth model by integrating UAS-derived leaf area index

Xuerui Guo [a,*], Bagher Bayat [a], Jordan Steven Bates [a,b], Michael Herbst [a], Marius Schmidt [a], Harry Vereecken [a], Carsten Montzka [a]

[a] Institute of Bio- and Geosciences: Agrosphere (IBG-3), Forschungszentrum Jülich GmbH, Jülich 52428, Germany
[b] Earth Observation and Ecosystem Modelling Laboratory, ULiège, Liège 4000, Belgium

ARTICLE INFO

Keywords:
GPP
NEE
RTM
LAI
AgroC
UAS

ABSTRACT

Accurate estimation of agroecosystem carbon fluxes is essential for assessing cropland sustainability and climate resilience. This study integrates Leaf Area Index (LAI) retrieval from Radiative Transfer Model (RTM) inversion into AgroC, an agroecosystem model, from Unmanned Aerial System (UAS) platform to enhance carbon fluxes estimates, including Gross Primary Production (GPP), Net Ecosystem Exchange (NEE), and Total Ecosystem Respiration (TER). By replacing the internally developed LAI in the AgroC model with interpolated LAI time series derived from UAS, improved spatiotemporal representativeness of agroecosystem carbon fluxes is observed under both the Farquhar-von Caemmerer-Berry (FvCB) and the Light Use Efficiency (LUE) photosynthesis approaches. Temporally, the highest GPP accuracy was achieved by the $AgroC_{FvCB}$ model integrated with UAS-derived LAI (RMSE = 3.19 gC m^{-2} d^{-1}, KGE = 0.89), while the best NEE estimation was obtained with the $AgroC_{LUE}$ model integrated with UAS-derived LAI (RMSE = 2.10 gC m^{-2} d^{-1}, KGE = 0.89). Spatially, the superior performance of the $AgroC_{FvCB}$ model in integrating UAS-derived LAI enabled high-resolution (1 m) mapping of GPP and NEE, effectively capturing within-field spatial variations in a winter wheat field. The daily Pearson correlation coefficient (r) overtime ranged from 0.16 in non-vegetated areas to 0.94 in vegetated zones for GPP, and up to 0.88 for NEE. Despite the advantages taking physical basis in RTM inversion for LAI retrieval and biochemical constraints considered in FvCB approach, the limitation in TER improvement requires further investigation to refine RTM-AgroC coupling for cropland carbon fluxes modelling using UAS platforms.

1. Introduction

Agroecosystems have dynamic and rapidly cycling active carbon pools, influenced by crop management, crop rotation, and soil health strategies, thus playing a critical role in the global carbon cycle (Frank et al., 2024; Lal, 2004). Accurately estimating two key carbon fluxes—gross primary production (GPP) and net ecosystem exchange (NEE)—is essential for evaluating agroecosystem sustainability as well as their impacts and resilience to climate change. GPP measures carbon fixation through photosynthesis, while NEE represents the net balance between carbon uptake and Total Ecosystem Respiration (TER). The eddy covariance (EC) flux tower provides continuous site-level carbon flux data (Baldocchi et al., 2001; Rebmann et al., 2018) by directly measuring NEE and partitioning it into GPP and TER using additional modelling approaches (Pastorello et al., 2020). These half-hourly records provide detailed insights into diurnal and seasonal carbon flux fluctuations at the EC site level. However, the spatial coverage of EC flux towers is sparse, limiting their ability to estimate dynamic carbon fluxes across large agroecosystem areas (Chu et al., 2021; Storm et al., 2023).

Several models have been developed to estimate GPP and NEE in agroecosystems. Light use efficiency (LUE) approach, e.g., implemented in land surface models (LSM), are among the widely used methods utilizing remote sensing observations for GPP monitoring at regional and global scales (Lawrence et al., 2019; Wolanin et al., 2019; Xiao et al., 2019; Yuan et al., 2010). However, the lack representation of cropland sites and broad categorization of rotational agricultural systems into single cropland plant functional type (PFT) introduces uncertainties in agroecosystem carbon flux estimates, often resulting in the underestimation of cropland GPP (Boas et al., 2021; Krause et al., 2022; Shirkey et al., 2022; Wang et al., 2013; Yuan et al., 2010; Zhang et al., 2017).

* Corresponding author.
E-mail addresses: x.guo@fz-juelich.de (X. Guo), b.bayat@fz-juelich.de (B. Bayat), J.Bates@uliege.be (J.S. Bates), m.herbst@fz-juelich.de (M. Herbst), ma.schmidt@fz-juelich.de (M. Schmidt), h.vereecken@fz-juelich.de (H. Vereecken), c.montzka@fz-juelich.de (C. Montzka).

https://doi.org/10.1016/j.agrformet.2025.110776
Received 9 April 2025; Received in revised form 29 July 2025; Accepted 6 August 2025
Available online 29 August 2025

Furthermore, seasonal variations such as crop phenology and dynamic carbon allocation, are inadequately represented in plant carbon cycling within many LSMs, which hampers the accurate mapping of crop site NEE (Boas et al., 2021; Lian et al., 2023; Post et al., 2017; W. H. Zhang et al., 2023).

In contrast, crop growth models (CGMs) embedded in agroecosystem models simulate crop growth dynamics including detailed species-specific physiological processes, such as phenology, nutrient limitations, and management practices (e.g., irrigation, fertilization) (Brilli et al., 2017; Friend, 1995; Liu et al., 2024; Paustian et al., 2019; Zhou et al., 2021). These models estimate carbon fluxes mechanistically, with photosynthesis in C3 plants commonly represented by the Farquhar-von Caemmerer-Berry (FvCB) model (Farquhar et al., 1980) and its derivatives (Bernacchi et al., 2001; Collatz et al., 1992; Farquhar et al., 2002). Coupled with CGMs, these agroecosystem models estimate leaf-level photosynthesis by considering biochemical constraints such as electron transport and Rubisco-limited carboxylation and then scale it up to canopy-level photosynthesis based on simulated green leaf area development. Among these agroecosystem models, the AgroC model (Herbst et al., 2008; Klosterhalfen et al., 2017) is one of the few that explicitly incorporates agroecosystem carbon flux pathways, e.g., it considers root exudates as a source of carbon transferred from plants to soil. It has also been reported to provide reliable estimates of NEE at the point scale (Herbst et al., 2021). However, despite its ability to close the one-dimensional carbon cycle between soil, plants, and the atmosphere, the AgroC model, like most CGMs, lacks spatial representation and typically requires site- and species-specific parameters, making it difficult to apply for large-scale monitoring and mapping of cropland carbon fluxes.

Unmanned aircraft system (UAS) has emerged as a valuable tool for more precise and field-specific assessment of crop dynamics due to their ability to capture high-resolution imagery with flexible operating times, minimal atmospheric interference and low survey costs. UAS also provides opportunities for the integration of LSMs and CGMs at the field scale, effectively balancing the broad spatial applicability of LSMs with the detailed plant functional mechanisms of CGM (Drees et al., 2024; Vigneault et al., 2024). In particular, the integration of Leaf Area Index (LAI) derived from UAS observations into CGM has received increasing attention as a means of linking retrieved canopy characteristics to mechanistic plant biophysical processes (Bukowiecki et al., 2024; Chen et al., 2022; Guo et al., 2024; Tang et al., 2023).

LAI, which determines the effective area of plant-atmosphere carbon and water exchange, serves as a key indicator of leaf growth and crop phenological status under environmental stress (Guo et al., 2021; Van Dijke et al., 2020; Yue et al., 2023). Methods for retrieving LAI from optical sensors can be broadly categorized into two approaches: data-driven empirical statistical approaches and physical-based radiative transfer model (RTM) inversion (Fang et al., 2019a). Data-driven approaches rely on empirical relationships between LAI and canopy spectral observation, primarily through vegetation indices (VIs), whereas RTM inversion is based on the physical laws of radiation and photons interactions to estimate LAI from spectra. Among RTMs, PROSAIL—a combination of the PROSPECT leaf optical property model (Jacquemoud and Baret, 1990) and the SAIL canopy reflectance model (Verhoef, 1998, 1984; Verhoef et al., 2007) — is widely used for LAI. It has been applied to generate LAI products across a wide range of satellite sensors (Brown et al., 2020; García-Haro et al., 2018; Li et al., 2015; Weiss et al., 2020; Yan et al., 2018) and scales (Bayat et al., 2018, 2016).

Nevertheless, UAS-based crop LAI estimation is primarily used for data assimilation, parameterization and site-specific calibration of crop models, with the target variables typically being static biomass or yield (Khodjaev et al., 2024; Meiyan et al., 2022; Peng et al., 2021; Tao et al., 2020; Zhou et al., 2017). Moreover, most current UAS-based crop LAI estimations rely heavily on empirical vegetation index (VI) models (Bates et al., 2021; Bukowiecki et al., 2024; Gong et al., 2021; Li et al., 2025; Putkiranta et al., 2024; Yang et al., 2023), while physical RTM inversion has been primarily explored using UAS-mounted hyperspectral sensors (Chakhvashvili et al., 2022; Duan et al., 2014; Guo et al., 2023; Jin et al., 2025; Yu et al., 2017). Although some studies have investigated LAI retrieval using UAS-loaded multispectral sensors with physical RTM inversion (Chakhvashvili et al., 2022; Sun et al., 2021; Verger et al., 2014), to the best of our knowledge, no study has explicitly integrated UAS-derived LAI obtained through RTM inversion into CGMs to investigate its ability to estimate carbon fluxes in the agroecosystem, including GPP, NEE, and TER. Therefore, we propose to integrate UAS-derived LAI obtained by RTM inversion using a UAS-mounted multispectral sensor with CGMs through the AgroC model. This integration aims to comprehensively evaluate its ability to capture the spatiotemporal dynamics of agroecosystem carbon fluxes.

2. Materials and methods

The study follows a workflow structured as shown in Fig. 1. First, various types of data are collected, including UAS imagery, ground-measured LAI values, and processed EC flux tower records of GPP, NEE, and TER. Next, LAI values are retrieved from UAS data using the RTM model PROSAIL inversion through a Look Up Table (LUT) approach. The retrieved LAI values are validated within the ground sampling area, and an interpolated time series of the retrieved LAI is integrated into the crop growth scheme within the AgroC model. Four versions of the AgroC model are implemented and evaluated, considering two types of photosynthesis pattern (i.e., LUE and FvCB) and the source of the LAI information—either internally developed from original versions or UAS-derived. Finally, the simulated carbon fluxes are then evaluated against EC flux tower observations at daily frequence using various performance metrics to identify the best-performing version of the AgroC model. This best-performing AgroC version is subsequently applied pixel-by-pixel within the study area to map carbon fluxes.

2.1. Data

2.1.1. Study site description and ground-based measurements

The experimental site is a 9.7 ha agricultural field in the River Rur catchment basin close to Selhausen, Germany (50°51′57’’N, 6°26′50’E). This field is recognized as a typical cropland PFT designated as DE-RuS by the Integrated Carbon Observation System (ICOS) (Rebmann et al., 2018) and TERrestrial ENvironmental Observatories (TERENO) network (Bogena, 2016). The sampling area including four continuous sampling plots (CPs) namely CP02, CP03, CP04 and CP05, are arranged in a circular configuration around the centrally located EC flux tower (Fig. 2). Additionally, a rectangular study area of approximately 0.3 ha in the centre surrounded by the EC flux tower was selected for carbon flux mapping in this study.

The field is situated at an elevation of 103 m above sea level and features a gentle southwest-facing slope of 0.3° The soil primarily comprises Pleistocene loess and Holocene migratory loess, underlain by a shallower gravel layer. Within the study area, the soil properties exhibit minimal differences in texture and horizontal distribution (Brogi et al., 2021). The region experiences a maritime temperate climate, with an average annual temperature of 10.0 °C and an average rainfall of 698.0 mm.

In recent years, the field and its neighbouring farmlands have followed a crop rotation system alternating between sugar beet and winter cereals. For the 2019–2020 growing season, the target crop was the winter wheat variety RGT Reform (*Triticum aestivum*), grown from 26 October 2019 to 28 July 2020.

The EC flux tower, along with other in-situ sensors, provides continuous measurement of a range of meteorological variables, including air temperature, relative humidity, wind speed, atmospheric pressure, and records of water, heat and carbon fluxes. Additional on-site hydrological data, such as soil temperature and moisture measurements at different soil depths, are available through participation in

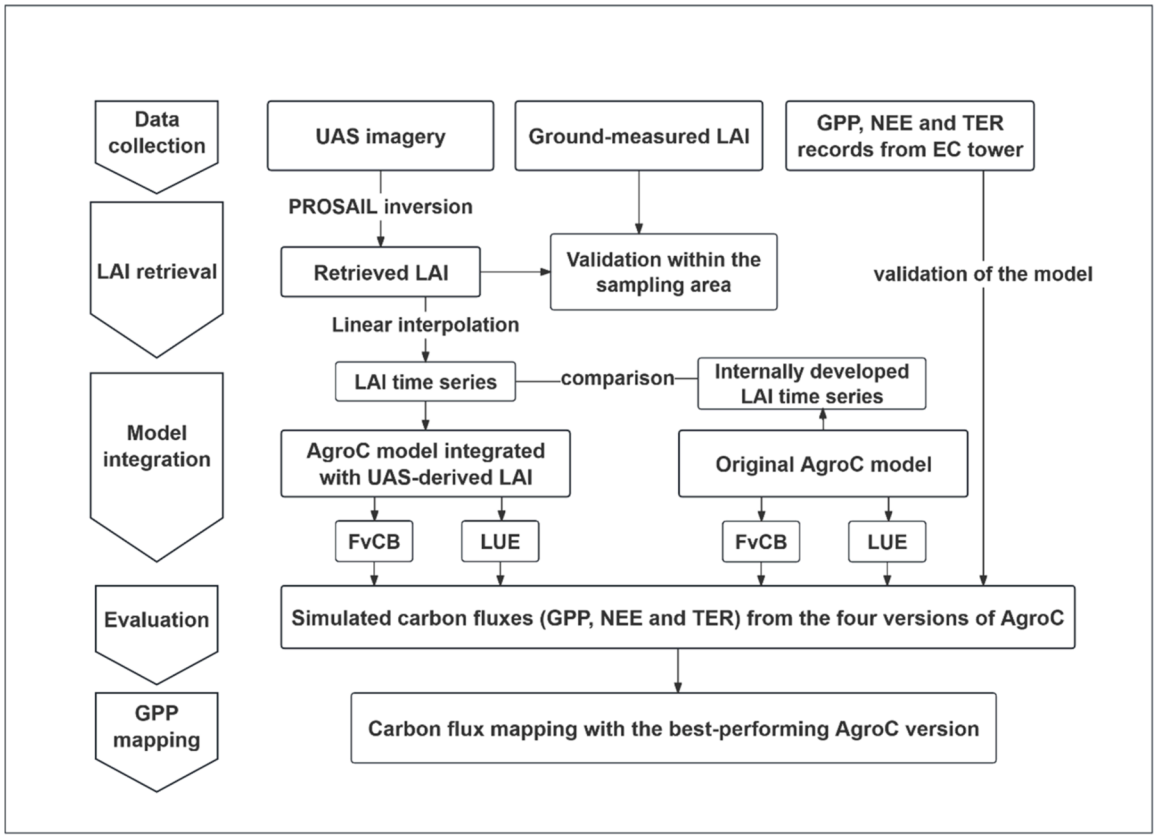

Fig. 1. Overview of the study workflow. The two alternative photosynthesis subroutines are shown as FvCB and LUE, namely the Farquhar-von Caemmerer-Berry and the Light Use Efficiency approaches.

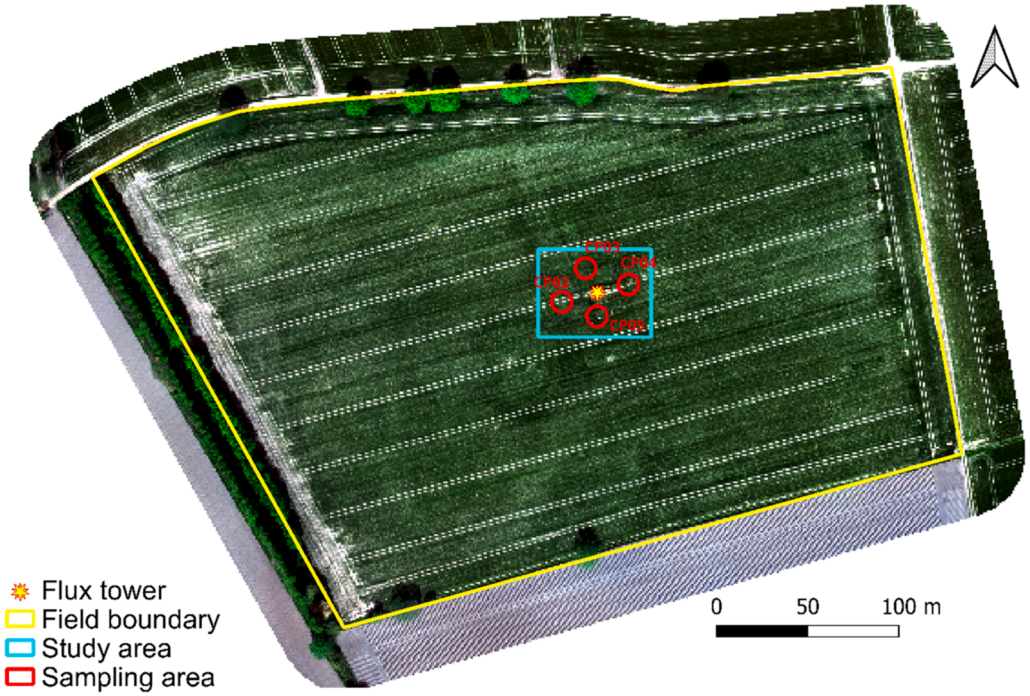

Fig. 2. Location of the ICOS field indicated with the yellow boundary and the sampling area centred around the EC flux tower. The background is the resampled 1 m RGB composite image taken on 16 April 2020 by UAS.

TERENO. Ground-based LAI measurements were conducted regularly within the sampling area throughout the growing season in accordance with the ICOS protocol (Gielen et al., 2018) using a SunScan Canopy Analysis System (Delta-T Devices Ltd, Cambridge, UK). The post-processing of the meteorological and carbon flux measurements is comprehensively outlined (Pastorello et al., 2020) and published as level

2 products on the ICOS data portal (ICOS, 2023). The LAI measurements also published as ancillary measurements at the DE-RuS site (Schmidt et al., 2025). A detailed description of the in-situ sensor measurement and variables in ICOS and TERENO product used in this study are presented in Table 1. The variable categories of meteorology, soil climate and radiation were primarily used as inputs to the AgroC model, while the carbon flux records were used for validation.

2.1.2. The UAS field campaign

The UAS field campaign was conducted using a Micasense RedEdge-M multispectral sensor (MicaSense, 2017) mounted on a DJI Matrice 600 hexacopter (DJI Technology Co., Ltd, Shenzhen, China). The multispectral sensor capture data in five bands: blue (475 nm ± 10 nm), green (560 nm ± 10 nm), red (668 nm ± 5 nm), red-edge (717 nm ± 5 nm) and near infrared (NIR) (840 nm ± 20 nm). A total of five valid UAS field campaigns were conducted on 16 April, 26 May, 23 June, 2 July and 9 July, covering the dominant winter wheat growing season. All the flights were conducted at an altitude of 100 m, with a degree of overlap of approximately 90 % and a flying speed of 6 m/s, under clear sky conditions between 10:00 and 14:00 local time. The Micasense RedEdge-M equipped with field of view (FOV) of 46°and a focal length of 5.4 mm, resulting in a Ground Sampling Distance (GSD) of 0.07 m. The sensor was positioned at nadir above canopy during each flight, and a reference white panel was photographed before taking off for radiometric calibration. The pre-processing procedures, including image alignment, radiometric processing and calibration, were carried out using the agricultural mode in the Pix4Dmapper software (PIX4Dmapper, 2017).

2.2. Method

2.2.1. LAI retrieval from PROSAIL model inversion

The Look-up table (LUT) approach was implemented for LAI retrieval using the PROSAIL-D model, which is the combination of PROSPECT-D (Féret et al., 2017) leaf optical model and SAIL (Verhoef, 1998, 1984; Verhoef et al., 2007) canopy model. The PROSPECT-D model advances in its consideration of leaf anthocyanin, allowing the simulation of the optical properties of leaves throughout their life cycle, from juvenile to senescent stages, as well as their response to environmental stress (Féret et al., 2017). The LUT generates a table of precomputed canopy reflectance spectra by forward-operating the PROSAIL-D model with a range of user-defined input parameters. An iterative minimization algorithm, using Root Mean Squared Error (RMSE) as the cost function, was employed to identify the simulated spectra that best matched the observed canopy spectra.

A total of 5000 simulated canopy spectra were generated using user-defined truncated normal distributions (with mean and standard deviation) for most of the PROSAIL-D input parameters (Table 2). To address the ill-posed issue, which refer to the situations where different parameter combinations can produce identical spectra simulations, prior knowledge of value range and distribution was incorporated into the input parameters (Berger et al., 2018; Danner et al., 2019; Féret et al., 2019, 2017; Kong et al., 2016; Schiefer et al., 2021). However, for the LAI parameter, the value ranges and distributions follow the in-situ measurements (Schmidt et al., 2025) and previous inversion studies (Danner et al., 2017; Huang et al., 2019). For more detailed information about the parameter ranges and distributions, the reader is referred to Table 2. To represent a default nadir observation in mid-high latitude summer, the solar zenith angle *tts*, viewing zenith angle *tto*, and relative azimuth angle *psi* were set to 30°, 0°, and 0°, respectively.

Furthermore, the spectral response function provided by the MicaSense RedEdge-M sensor manufacturer (MicaSense, 2017) was used to resample the continuous simulated spectra to five discrete spectral bands. The resampling process accounted for weight differences in spectral responses. The implementation was carried out using the ***prospect*** package in R (Féret and de Boissieu, 2024).

Table 1
Description of the variables in the ICOS Level 2 product at DE-RuS site used in this study.

Symbol	Description	Unit	Category
GPP_DT_VUT_REF	GPP from Daytime partitioning method, reference selected from GPP versions using model efficiency (MEF).	μmolCO_2 m^{-2} s^{-1}	Carbon flux
NEE_VUT_REF_JOINTUNC	Joint uncertainty estimation for NEE_VUT_REF, including random uncertainty and USTAR filtering uncertainty.	μmolCO_2 m^{-2} s^{-1}	Carbon flux
TA_F	Air temperature, consolidated from TA_F_MDS* and TA_ERA data.	°C	Meteorology
TS_F_MDS_1*	Soil temperature at surface layer.	°C	Soil climate
TS_F_MDS_6*	Soil temperature at the bottom of the soil profile.	°C	Soil climate
P_F	Precipitation consolidated from P and P_ERA.	mm	Meteorology
SW_IN_F	Shortwave incoming radiation.	W/m^2	Radiation
RH	Relative humidity.	%	Meteorology
PA	Atmospheric pressure.	kPa	Meteorology
WS	Wind speed.	m/s	Meteorology

* The suffix represents the processing method, for example the Marginal Distribution Sampling (MDS) used gap filling is identified by the _F_MDS suffix and _ERA represent the ERA-Interim reanalysis data product. More information could be found in (Pastorello et al., 2020).

2.2.2. The AgroC model

The AgroC model is a numeric model designed to simulate agroecosystem carbon dynamics. It integrates three modules, the Simple and Universal Crop growth Simulator (SUCROS) (Spitters et al., 1989) for crop growth and development, the SoilCO2 model (Šimůnek and Suarez, 1993) for the transfer and production of soil carbon fluxes, and the Rothamsted Carbon Model (RothC) (Coleman and Jenkinson, 1996; Smith et al., 1997) for soil organic carbon turnover. Given that the green leaves area within the AgroC model is functionally consistent with the remote sensing inverted LAI, the green leaf area simulated in the AgroC model is regarded as LAI in the following text.

The simulation of plant organ growth within the AgroC model, including the development of internal LAI, follows the SUCROS framework and is determined by pre-defined initial parameters and tables of net dry matter allocation at different developmental stages (DVS). For instance, the LAI initially follows exponentially growth from a set initial ear area leaf area (EAI), depending on the effective temperature and a given relative growth rate (RGR), until the leaves become competitive for light, typically defined as a developmental stage (DVS) of 0.3 or a total leaf area of 0.75. Thereafter, the rate of LAI expansion during the stationary growth period is determined by the net dry matter allocated to the leaves. In addition, the development of the DVS is affected by the cumulative daytime temperature and is represented by a continuous number, with 0 representing sowing, 1 representing flowering and 2 representing maturity.

The AgroC model has incorporated both the LUE method (Herbst et al., 2008) and the FvCB method (De Cannière et al., 2021) as interchangeable options for simulating photosynthesis, i.e., rate of CO_2 assimilation, which determines the gross dry matter accumulation. The LUE approach relates photosynthesis rate to the amount of the absorbed photosynthetically active radiation (APAR), while the FvCB approach introduces more biophysical constraints. The three dominant

Table 2
Input variables and their distributions for LUT generation from PROSAIL-D models.

Model	Symbol	Description	Range (Mean, Stdv)	Unit	References
PROSPECT-D	N	Leaf structure parameter	1.0 – 2.5 (1.6,0.3)	*Unitless*	Range from (Berger et al., 2018)
	C_{ab}	Chlorophyll a + b Content	0 – 80 (44.8,12.2)	$\mu g/cm^2$	Range from (Berger et al., 2018) and distribution from (Danner et al., 2019)
	CAR	Carotenoid content	0 – 25.28 (8.84, 5.14)	$\mu g/cm^2$	Range and distribution from (Féret et al., 2017)
	ANT	Leaf Anthocyanin content	0.56 – 2.81 (1.23,0.36)	$\mu g/cm^2$	Range and distribution from (Schiefer et al., 2021)
	EWT	Equivalent water thickness	0.004 – 0.034 (0.0203,0.0062)	*cm*	Range from (Féret et al., 2019) and distribution from (Danner et al., 2019)
	LMA	Leaf mass per area	0.00166 – 0.0331 (0.005575,0.0008)	g/cm^2	Range from (Féret et al., 2019) and distribution from (Danner et al., 2019)
	BROWN	Brown pigments content	0 – 1 (0.17,0.31)	*Unitless*	Range and Distribution from (Danner et al., 2019)
4SAIL	LAI	Leaf area index	0 – 8 (3.96,2.00)	m^2/m^2	Range from (Berger et al., 2018; Danner et al., 2017; Huang et al., 2019) and distribution from (Danner et al., 2019)
	q	Hot spot parameter	0.1	*Unitless*	Default
	LIDFa	Average Leaf Inclination Angle	25 – 78 (61,13)	*deg*	Range and distribution from (Danner et al., 2019)
	psoil	Soil reflectance	0.5	*Unitless*	Site-based adjustment and assumed to be Lambertian
	tts	Solar zenith angle	30	*deg*	Default
	tto	Viewing zenith angle	0	*deg*	Default
	psi	Relative azimuth angle	0	*deg*	Default

components, as shown in Eq. (2), are grouped as light limitation, Rubisco limitation and water limitation, from left to right, according to the major limiting variables. Apart from the light limitation by APAR, the Rubisco limitation involved the maximum carboxylation rate *VCmax*, and the water limitation reflects the influence of water availability based on the internal leaf partial pressures for CO_2 and O_2.

The respiration processes in the AgroC model consist of growth respiration, maintenance respiration, and heterotrophic respiration (HR), which together as TER and regulate the carbon balance between GPP and NEE. The growth and maintenance respiration are directly linked to organ-specific development. In contrast, the HR, which represents CO_2 production by soil microorganisms, follows the turnover of organic carbon pools as modelled by the RothC scheme.

$$\boldsymbol{GPP_{LUE}} = \boldsymbol{AMAX} - \left(1 - \boldsymbol{e}^{-\frac{\boldsymbol{EFF}*\boldsymbol{APAR}}{\boldsymbol{AMAX}}}\right) \cdot \overline{\boldsymbol{a}} \cdot \boldsymbol{f}(\boldsymbol{LAI}) \tag{1}$$

$$\boldsymbol{GPP_{FvCB}} = \boldsymbol{min}\left(\frac{4.6\cdot\boldsymbol{\zeta}\cdot(\boldsymbol{c_i} - \boldsymbol{\Gamma}^*)\cdot\boldsymbol{APAR}}{\boldsymbol{c_i} + 2\cdot\boldsymbol{\Gamma}^*}, 0.5\cdot\boldsymbol{VCmax}, \frac{\boldsymbol{VCmax}\cdot(\boldsymbol{c_i} - \boldsymbol{\Gamma}^*)}{\boldsymbol{c_i} + \boldsymbol{K_c}\cdot(1 + \boldsymbol{o_i}/\boldsymbol{K_o})}\right) \cdot \boldsymbol{f}(\boldsymbol{LAI}) \tag{2}$$

$$\boldsymbol{VCmax} = \overline{\boldsymbol{a}}\cdot\boldsymbol{VCmax}, 25\cdot\boldsymbol{f}(\boldsymbol{T_{air}}) \tag{3}$$

Where *APAR* represents the absorbed photosynthetically active radiation, while $\overline{a}$ stands for water stress. *AMAX* and *EFF* refer to the maximum photosynthetic capacity at light saturation and initial light use efficiency, respectively. ζ is the quantum efficiency, and Γ^* is the compensation point. $f(LAI)$ describes the partitioning of the total green leaf area into sunlit and shaded leaf areas. c_i and o_i represent the internal leaf partial pressure for CO_2 and O_2, respectively. K_c and K_o are the Michaelis-Menten constants for CO_2 and O_2. Finally, *VCmax* and *VCmax*, 25 denote the real time maximum rate of carboxylation and the maximum rate of carboxylation at 25°, respectively.

In this study, four versions of the AgroC model were tested and evaluated, considering two photosynthesis modes (i.e., LUE and FvCB) and the source of LAI information - original internally developed or UAS-derived. The UAS-derived LAI values were integrated into the AgroC model using a forcing approach. This method directly replaced the internally developed LAI with a linear interpolation of the UAS-derived LAI for each available date, ensuring the same temporal consistency as the internal AgroC simulations. The four versions of the AgroC model were initially operated with the average conditions within the sampling area, in which the area average of the UAS-derived LAI was incorporated. The most optimal AgroC model version was then selected and applied pixel by pixel over the entire study area at a 1 m resolution. For both point-level and area-level operations, the AgroC model was executed at hourly intervals within a one-year loop from 1 October 2019 to 30 September 2020.

The AgroC model incorporated plant-related inputs and initial parameters for the LUE approach that align with the standard winter wheat crop settings, which largely adhere to the default settings of the SUCROS model (Spitters et al., 1989; Van Laar et al., 1997) and a site-specific adjustment based on a calibration study (Klosterhalfen et al., 2017). In addition, the two initial reference parameters required for the FvCB approach— *VCmax*, 25 and the Ball-Berry stomatal parameter *m* —were set to 80 and 7, respectively, according to literature (Sulis et al., 2015). Furthermore, the soil material and hydraulic parameters are averages that represent the rectangular study area according to a geophysical survey (Brogi et al., 2021). Notably, the effect of water stress $\overline{a}$ on the photosynthesis rate indicated in Eq. (1) and Eq. (3) further affects the total dry matter accumulation, which consequently impacts the internal LAI development in the AgroC model. To ensure a comprehensive comparison of the LAI from disparate sources, no water stress was applied in the AgroC versions with UAS-derived LAI incorporated and $\overline{a}$ was assigned to its maximum value of 1.

The hourly meteorological inputs of the AgroC were primarily aggregated from the ICOS Level 2 products at the DE-RuS site, except for the potential evapotranspiration (ET_0), which was calculated using the Penman-Monteith method according to the FAO56 (Allen et al., 1998). Other required site management details, including sowing and harvest dates, were provided by the local farmers. A detailed description of the input settings for the AgroC model can be found in Appendix A.

2.2.3. Model performance evaluation

The performance of the AgroC model in estimating temporal carbon fluxes was evaluated using a set of key metrics. The Kling-Gupta Efficiency (KGE) and its three components (Pearson correlation coefficient *r*, variability α and bias β) (Gupta et al., 2009) were selected, as KGE provides a more comprehensive evaluation of model performance than traditional metrics like R^2. Specifically, it captures not only the strength

of correlation but also the variability and bias between simulated and observed dataset, which are critical aspects when assessing time series of ecosystem fluxes such as GPP, TER, and NEE. In addition, the root mean squared error (RMSE) was also employed to quantify the overall magnitude of prediction error. For model evaluation, daily GPP and NEE observations from the ICOS dataset were used, while observed TER was estimated as the difference between NEE and GPP. To reduce uncertainty in TER evaluation, we excluded cases where the estimated TER was negative, in accordance with established practices in the literature (Noh et al., 2024; Sun et al., 2023).

The comparison was conducted between the measured and simulated carbon fluxes on an aggregated daily basis from 1 January 2020 until the harvest on 28 July 2020. This was due to insufficient simulated vernalization accumulation achieved prior to that time. In addition, to evaluate spatial variation, the Pearson correlation coefficient (r) between the ICOS observation and the AgroC simulations were visualized for each pixel within the study area.

$$\mathrm{KGE} = 1 - \sqrt{(r-1)^2 + (\alpha-1)^2 + (\beta-1)^2}$$

$$r = \frac{\Sigma_{i=1}^{n}(y_i - \bar{y}_i)(\hat{y}_i - \bar{\hat{y}}_i)}{\sqrt{\Sigma_{i=1}^{n}(y_i - \bar{y}_i)^2 \, \Sigma_{i=1}^{n}(\hat{y}_i - \bar{\hat{y}}_i)^2}}$$

$$\mathrm{RMSE} = \sqrt{\frac{\Sigma(y_i - \hat{y}_i)^2}{n}}$$

where r is the Pearson correlation coefficient, which measures the linear correlation between the simulated and observed values. α is the variability, defined as the ratio of the simulated data standard deviation to the observed data standard deviation. β is the bias, calculated as the ratio of the simulated data mean to the observed data mean. y_i is the observed ground truth dataset, indicating the measured carbon fluxes from EC flux tower. $\hat{y}_i$ stands for the predict data, i.e. the carbon fluxes simulated from the AgroC model. $\bar{y}_i$ and $\bar{\hat{y}}_i$ represent the average value of y_i and $\hat{y}_i$, respectively. n is the total number of days in the comparison period.

3. Result

3.1. Temporal comparison in LAI and carbon fluxes

The UAS-derived LAI integration outperformed the internally developed LAI in both trend and peak detection when compared to the ground measurements (Fig. 3). The internally developed LAI in the $\mathrm{AgroC_{LUE}}$ and $\mathrm{AgroC_{FvCB}}$ versions estimated early peaks on 22 April and on 15 May, with peak values of 6.04 and 3.77, respectively. In contrast, the integrated UAS-derived LAI peaked on 26 May, with a peak value of 5.32, which was more consistent with the ground measured LAI peak of 5.02 on 28 May. The process-based developments on other processes, e.g., the DVS, are illustrated in Appendix B.

The AgroC model generally captured the seasonal variation of carbon fluxes in the sampling area (Fig. 4 and Fig. 5). The simulations of GPP and NEE (negative values indicate carbon uptake), showed significant improvements in both the $\mathrm{AgroC_{LUE}}$ and $\mathrm{AgroC_{FvCB}}$ versions after the integrating with UAS-derived LAI, which was reflected in lower RMSE

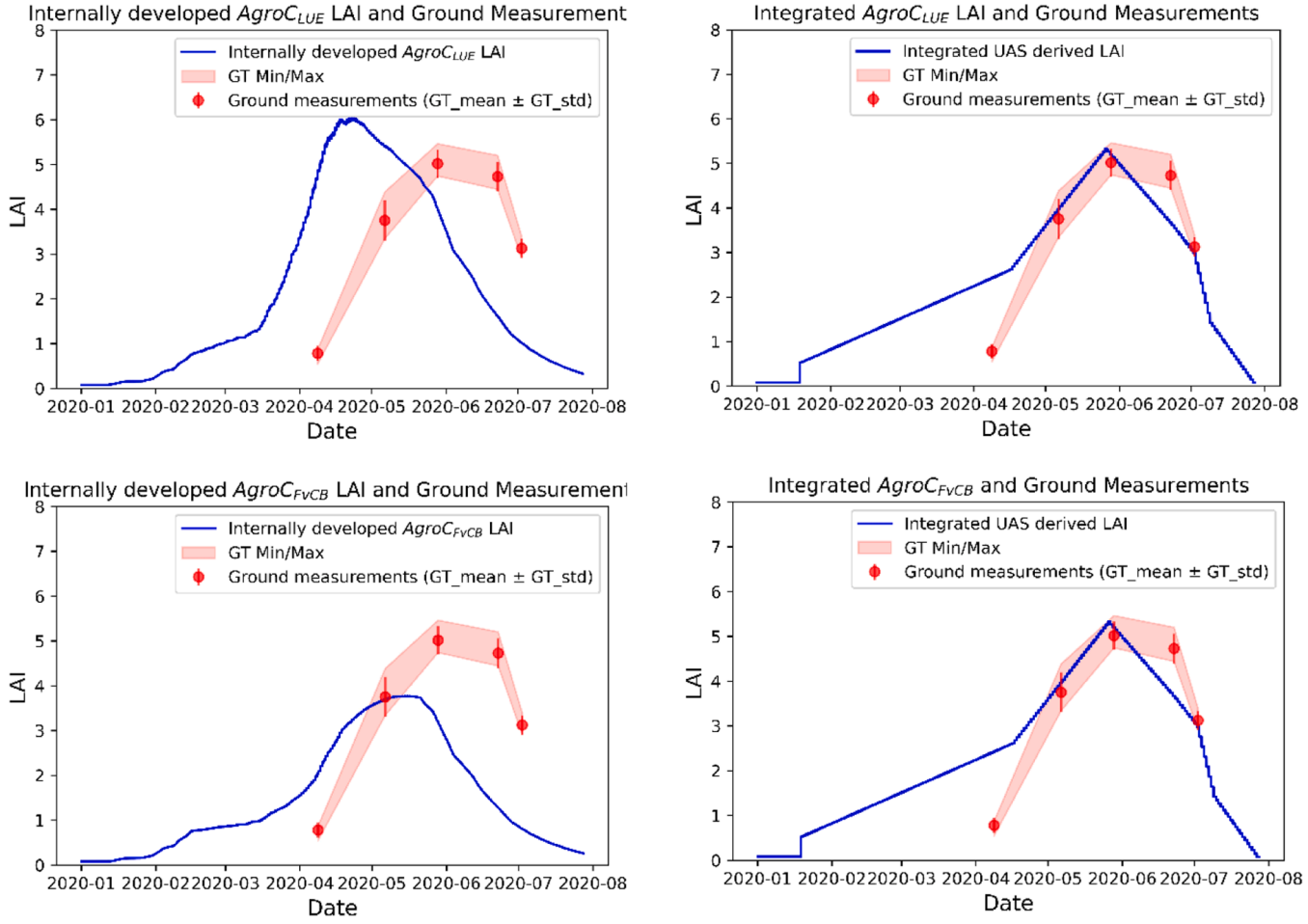

Fig. 3. The comparison of the LAI in different versions of the AgroC model.

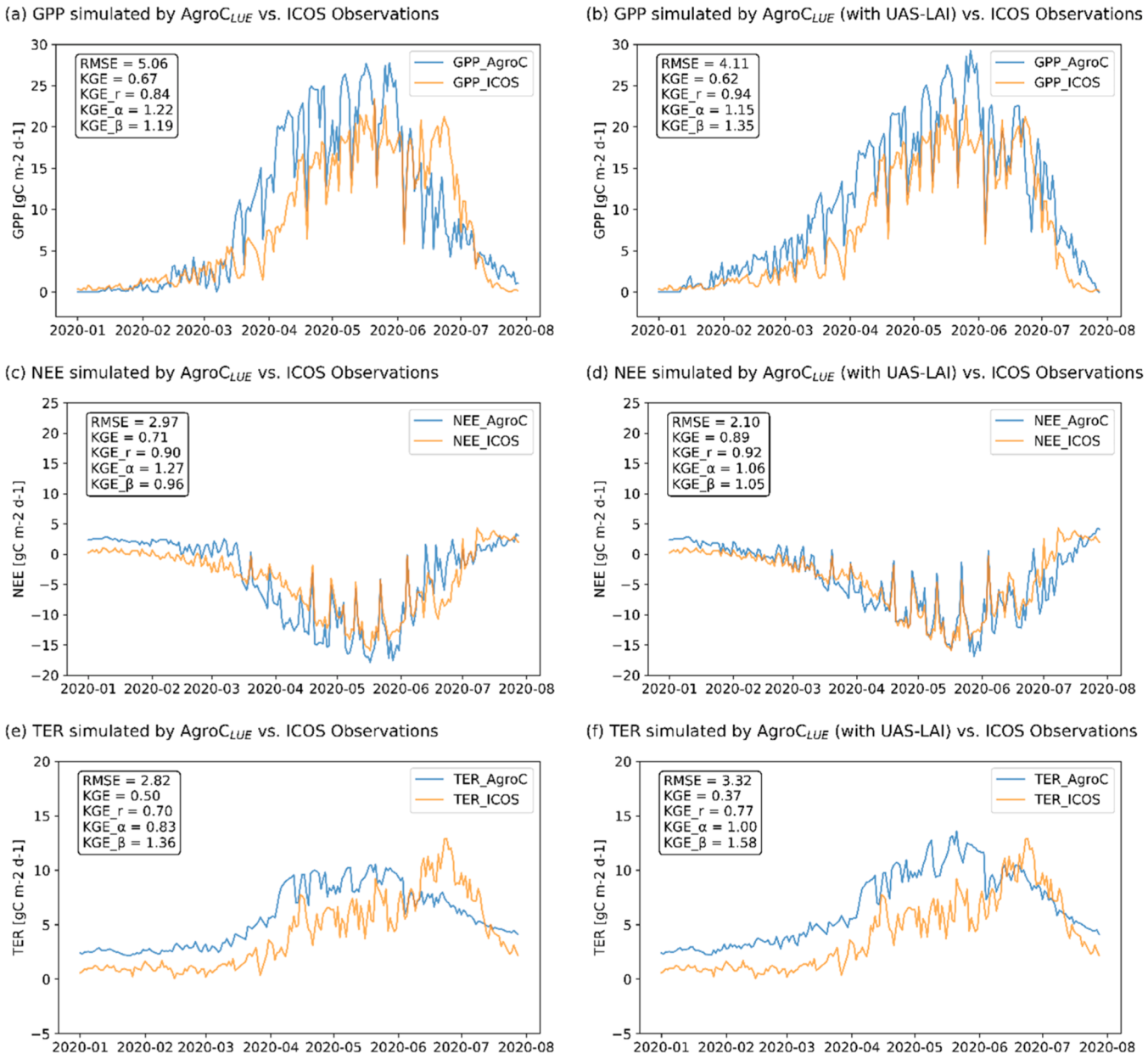

Fig. 4. Comparison of daily carbon flux time series simulated by the AgroC$_{LUE}$ model and ICOS measurements. The left column shows the simulation results of the original AgroC$_{LUE}$ model, and the right column shows the simulation results of the AgroC$_{LUE}$ model integrated with UAS-derived LAI.

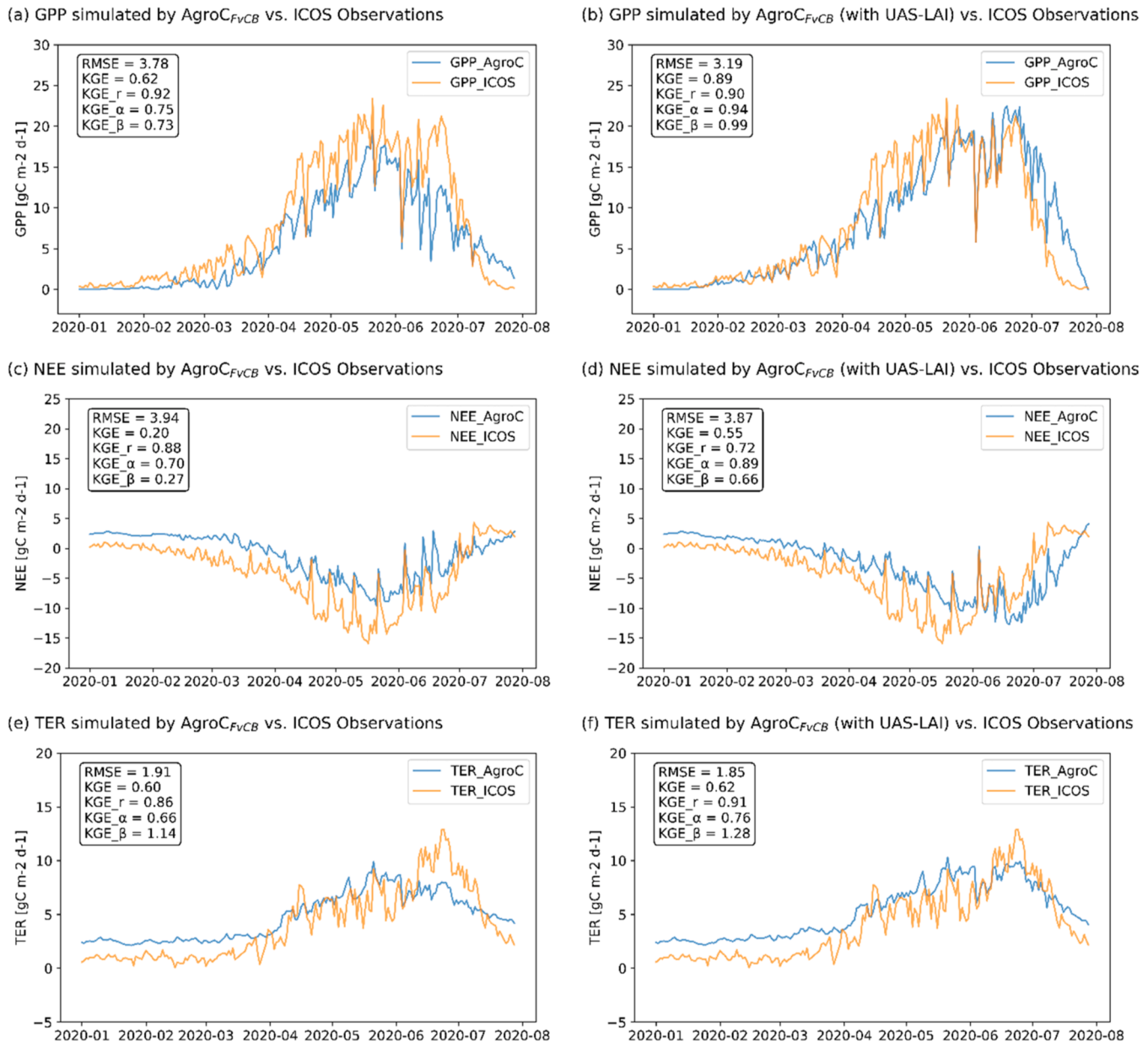

Fig. 5. Comparison of daily carbon flux time series simulated by the AgroC$_{FvCB}$ model and ICOS measurements. The left column shows the simulation results of the original AgroC$_{FvCB}$ model, and the right column shows the simulation results of the AgroC$_{FvCB}$ model integrated with UAS-derived LAI.

Table 3
Comparison of the accumulated carbon fluxes amount over the entire growing season from sowing to harvest with ICOS dataset.

Data source/AgroC version	Total GPP (gC m^{-2})	Total NEE (gC m^{-2})	Total TER (gC m^{-2})	GPP Bias (%)	NEE Bias (%)	TER Bias (%)
ICOS observation	1703.00	-792.04	922.42	–	–	–
Original AgroC$_{LUE}$	2001.62	-562.78	1402.89	17.53	28.94	52.09
AgroC$_{LUE}$ with UAS-derived LAI	2266.57	-635.49	1591.11	33.11	**19.78**	72.49
Original AgroC$_{FvCB}$	1226.63	21.19	1222.78	-27.98	102.68	**32.56**
AgroC$_{FvCB}$ with UAS-derived LAI	1672.28	-309.20	1334.09	**-1.81**	60.96	44.63

and KGE values closer to 1. Among the tested four configurations of AgroC model, the AgroC$_{FvCB}$ version incorporated with UAS-derived LAI demonstrated the best performance in GPP estimation (Fig. 5b), achieving the lowest RMSE of 3.19 gC m^{-2} d^{-1} and the highest KGE value of 0.89. Although the original AgroC$_{LUE}$ version incorporated with UAS-derived LAI achieved a higher r of 0.94 for GPP simulation (Fig. 4b) due to its improved correlation, a slightly better representation in variability and bias was obtain with the AgroC$_{FvCB}$ version with UAS-derived LAI (Fig. 5b), as evidenced by α and β values closer to 1. The AgroC$_{FvCB}$ with UAS-derived LAI also outperformed other configurations in TER estimation (Fig. 5f), with the lowest RMSE of 1.85 gC m^{-2} d^{-1} and the highest KGE value of 0.62. For NEE estimation, the AgroC$_{LUE}$ version incorporated with UAS-derived LAI performed the best (Fig. 4d), achieving the highest r of 0.92, lowest RMSE of 2.10 gC m^{-2} d^{-1} and the highest KGE value of 0.89. Additionally, the supplement scatterplots for each carbon flux comparison are listed in Appendix C (Fig. C.1 and Fig. C.2).

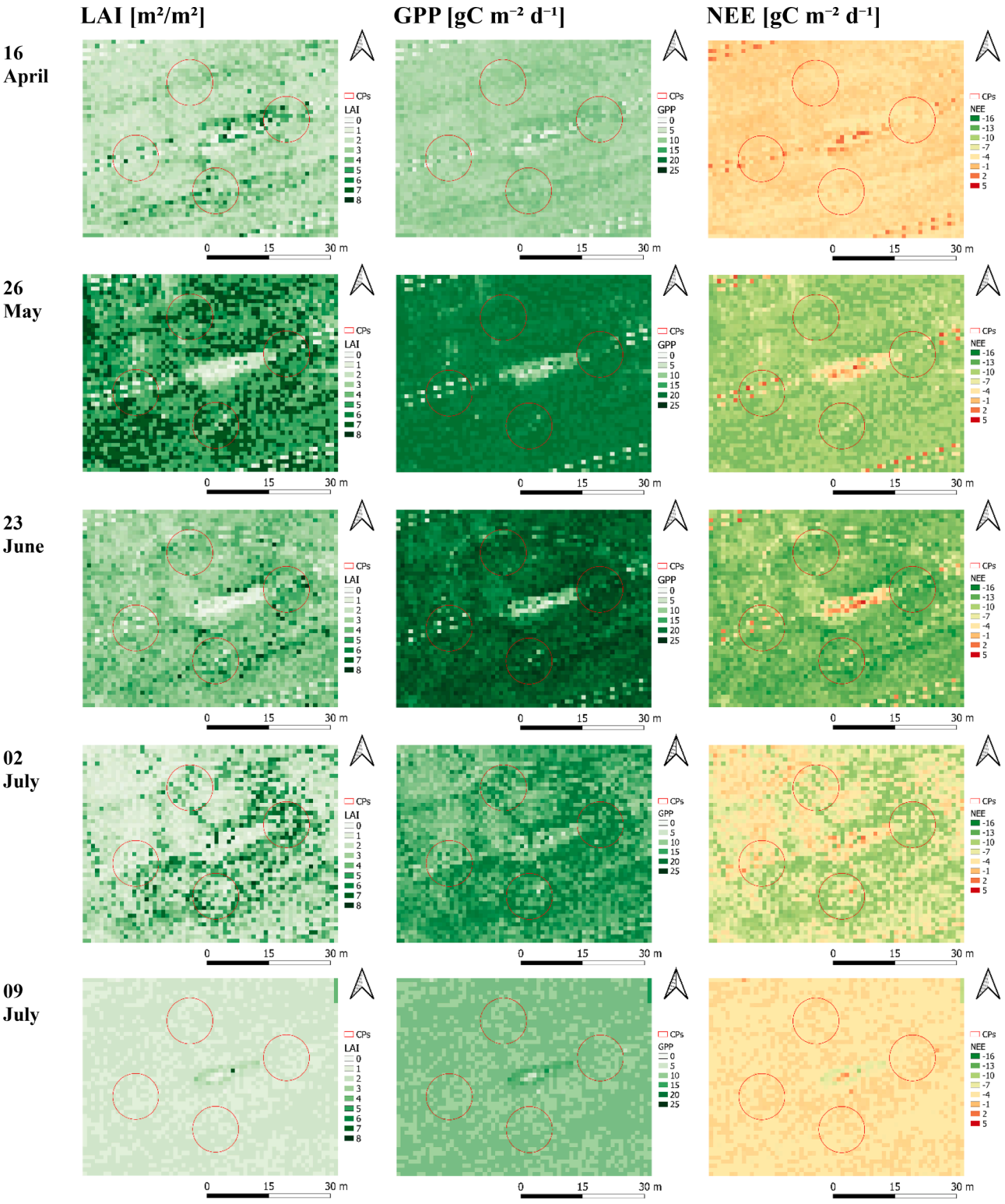

Fig. 6. The daily LAI, GPP and NEE mapping for UAS observation dates within the study area. The red circular boundaries represent the four continuous sampling plots (CPs).

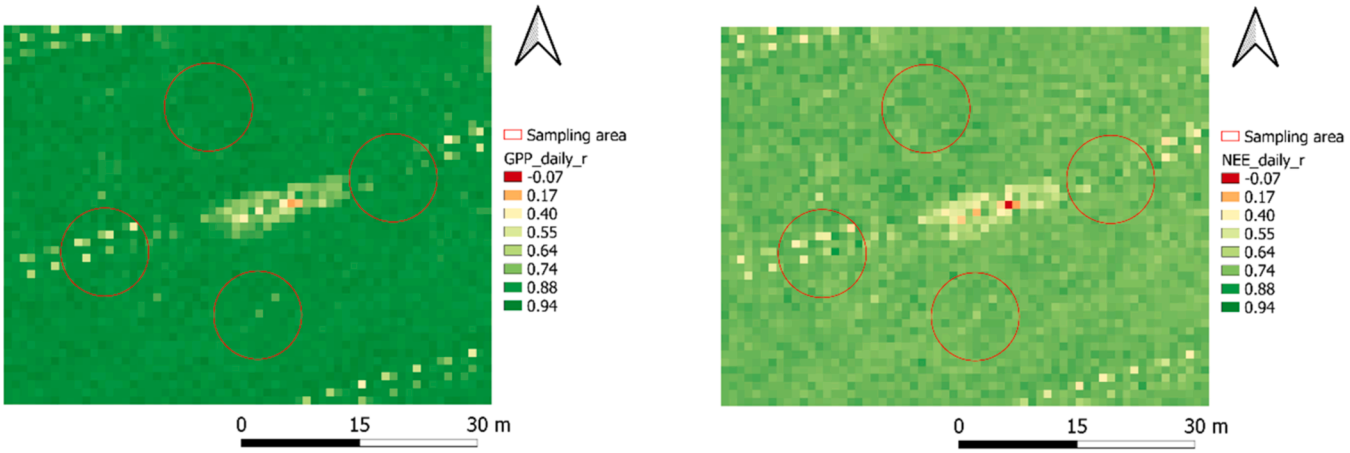

Fig. 7. Map of Pearson correlation coefficient (***r***) for daily GPP (left) and NEE (right) simulations over time from sowing to harvest, compared with the ICOS observations. The red circular boundaries represent the four continuous sampling plots (CPs).

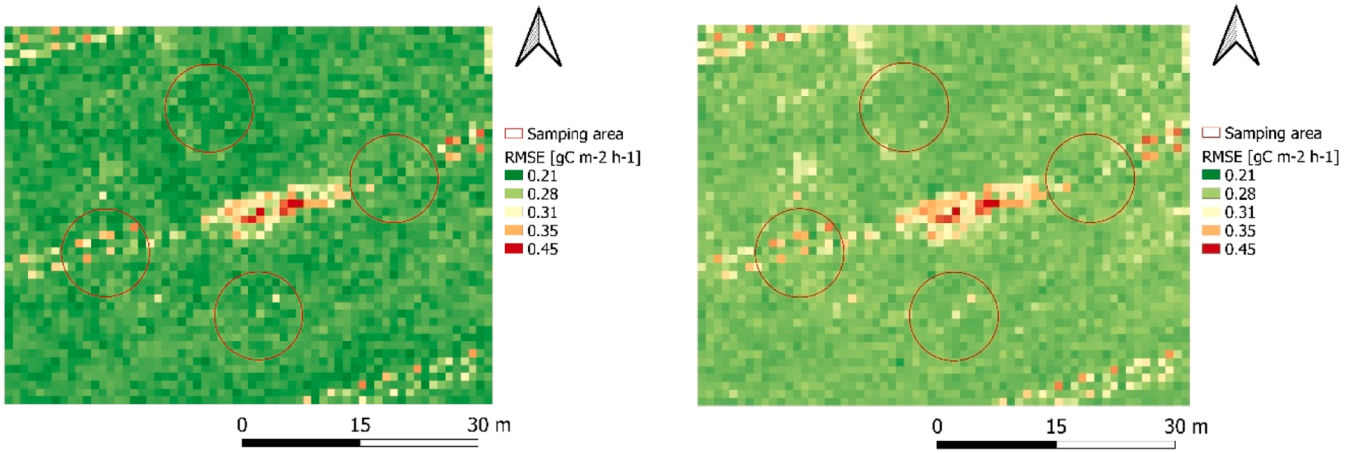

Fig. 8. Map of RMSE for hourly GPP (left) and NEE (right) simulations over time from sowing to harvest, compared with ICOS observations.

Furthermore, the improved accuracy of cumulative GPP and NEE from sowing to harvest was also found with UAS-derived LAI. The minimal bias of -1.81 % for GPP and 19.78 % for NEE, was both achieved with integrating UAS-derived LAI, compared to ICOS measurements during the 2019–2020 winter wheat growing season (Table 3). An overestimation of cumulative TER is generally observed in all four versions of the AgroC models, and the incorporation of LAI exacerbated this trend.

3.2. *Spatial variation of UAS-derived LAI and carbon fluxes*

The best-performing version $AgroC_{FvCB}$ with UAS-derived LAI integration was employed for pixel-by-pixel carbon flux mapping in the study area, as it achieved the best result in GPP capture. The carbon fluxes spatial variation matches visually with the LAI derived from the UAS imagery (Fig. 6). The lowest LAI and GPP values, as well as the positive NEE values for all the observation dates, are primarily located along the unvegetated tractor paths, the field ridge and the central equipment area. Moreover, the observed spatial variation is indicative of a phenology shift. For instance, the spatial variation for UAS-derived LAI, GPP and NEE on 2 July 2020 corresponded to spatial differences in the timing of winter wheat maturity across the field (Fig. 6). In addition, the spatial variation of the UAS-derived LAI among the four CPs observed in May and June, with a standard deviation of 0.46, was comparable to the 0.36 of the ground measurements.

The spatial variation in carbon fluxes also revealed in the daily *r* over time, with *r* for GPP ranging from 0.16 in non-vegetated areas to 0.94 in vegetated area and for NEE range from -0.07 to 0.88 (Fig. 7). The hourly RMSE map (Fig. 8) further accentuates this spatial discrepancy, with majority green vegetation area achieved RMSE less than 0.28 gC m^{-2} h^{-1} for GPP and NEE. It can be observed that the GPP in the striped vegetated areas in the northwest region exhibits a weaker correlation with the EC tower-measured GPP compared to those in the south, which also corresponds to lower LAI values, suggesting poor growth and early maturation.

4. Discussion

4.1. *UAS in LAI retrieval and cropland carbon fluxes simulation*

Our study demonstrates that UAS-mounted multispectral imagery enables accurate, high-resolution (1 m) LAI retrieval, effectively capturing winter wheat growth dynamics across all stages. The UAS-derived LAI closely matched ground measurements, with only a minor deviation—peaking just two days earlier and overestimating the maximum LAI by 6.15 % (0.31). This level of accuracy underscores the robustness of RTM inversion approach, particularly when compared to VI-derived LAI estimations using the same dataset (Bates et al., 2021), which severely underestimated peak LAI by 40.23 % (2.01). In addition, the enhanced performance of UAS-derived LAI in comparison to internally developed LAI within the AgroC model signifies that the retrieved LAI from UAS has advantages over crop growth simulations and avoids

crop model parameterization when applied over large spatial areas. This benefit is particularly pronounced in scenarios where substantial spatial variations are observed, such as during the mid-to-late growth stage, when there is a noticeable difference in maturity. The $AgroC_{LUE}$ model, which used site-calibrated, crop-specific parameters but did not include UAS-derived information, simulated a peak LAI of 6.04. This is slightly higher than the 5.6 reported for winter wheat at the same site in 2009 (Klosterhalfen et al., 2017). However, this is still within a plausible variation range, as the same study also documented that peak simulated LAI values could vary by up to 1.4-fold between normal and drought years at another winter wheat site. These findings underscore the role of climate-driven LAI interannual variability.

In addition to the benefits of accurate LAI retrieval, the integration of UAS-derived LAI into the AgroC model reduces the uncertainties in satellite-based GPP estimation and addresses the challenges of coarse resolution in capturing vegetation heterogeneity (Pacheco-Labrador et al., 2022). Despite the findings of prior studies indicating poorer carbon fluxes temporal monitoring at the DE-RuS site due to a lack of regional crop rotation data and limited access to high-quality satellite products (Du et al., 2022; Fang et al., 2019b; Liu et al., 2018), our approach demonstrates superiority in GPP and NEE estimates at the same test site. Our best-performing model ($AgroC_{FvCB}$ integrated with UAS-derived LAI) achieves superior accuracy in GPP simulation from sowing to harvest (R^2 = 0.85, RMSE = 2.78 gC m^{-2} d^{-1}, KGE = 0.91; results not shown), surpassing the reported leading satellite-driven LUE model (R^2 = 0.73, KGE = 0.76, RMSE = 3.0 gC m^{-2} d^{-1}) at the same DE-RuS site (Du et al., 2022). Additionally, our GPP estimates exhibit comparable accuracy to other satellite-driven GPP models that involve site-calibrated or crop-specific parameters, such as those by Jiang et al. (2021) (R^2 = 0.81, RMSE = 2.62 gC m^{-2} d^{-1}) and Meroni et al. (2019) (R^2 = 0.68, RMSE = 2.7 gC m^{-2} d^{-1}), while our model maintains higher hourly temporal resolution. Moreover, our best model underestimates GPP by a minimum of only 0.97 gC m^{-2} d^{-1} (4.3 %), outperforming another agroecosystem model, SPA-Crop model, tested on a winter wheat field (Revill et al., 2019), which exhibited an average underestimation of 5.2 gC m^{-2} d^{-1} (26 %) for GPP.

Our approach highlights the gaps in NEE spatiotemporal capture by combining UAS-derived LAI with the AgroC model, and our NEE temporal capture results at the DE-RuS site outperform those simulated from process-based LSMs. The default settings for the CLM-5 model and its winter wheat version CLM-WW result in higher RMSE values (8.03 and 7.86 gC m^{-2} d^{-1}, respectively) and lower correlation indicated by r (0.21 and 0.33) during the 2017/2018 winter wheat season at the DE-RuS site (Boas et al., 2021). In contrast, our best-performing model ($AgroC_{FvCB}$ integrated with UAS-derived LAI) model reduces this error to just 3.69 gC m^{-2} d^{-1} from sowing to harvest and achieves an average daily r of 0.78 (result not shown). Similarly, our approach performs well in capturing the accurate NEE amplitude, underestimating the peak by 3.16 gC m^{-2} d^{-1} (24.8 %), while another agroecosystem model SPA-Crop (Revill et al., 2019), reported an underestimate peak NEE by 6.2 gC m^{-2} d^{-1} (46 %).

In addition to temporal accuracy, our approach effectively captures within-field spatial variations in carbon fluxes. In purely vegetated regions, our NEE simulations are consistent with a multiple point-level study (Herbst et al., 2021), which reports correlation between hourly simulated and measured NEE over time ranging from 0.34 to 0.85 (average r = 0.66) across 15 sites within a sugar beet field. In comparison, our UAS-based estimates exhibited a similarly strong correlation with the ICOS measurements at hourly frequence, with pixel-level hourly r values ranging from 0.61 up to 0.88 and an average of 0.82 within the sampling area (see Appendix C Fig. C.3). Despite the negative Pearson correlation coefficient (r) in few non-vegetated pixels (Fig. 7) arises from the expected contrast between modelled daily CO_2 emissions (positive NEE, dominated by soil respiration) and tower-measured fluxes (negative NEE, dominated by vegetation uptake in surrounding vegetated zones). This spatial mismatch does not indicate a model bias but rather reflects differing land cover contributions—a phenomenon supported and explored in several studies (Bellucco et al., 2017; Nordbo et al., 2012). Moreover, the boundaries with large differences in the r and RMSE mapping are similar to the soil property boundaries between the soil type C1a and C1b reported in a land survey (Brogi et al., 2021, 2020). The former soil type generally exhibits higher average r values and lower average RMSE values for hourly GPP and NEE statistics. These findings suggest that spatial variations in LAI-driven GPP are strongly linked to subsurface soil properties and demonstrate that the addition of UAS-based LAI inversion can eliminate the need for site-specific parameter tuning in crop growth modelling. However, given the relatively minor soil heterogeneity and single-season experiment that was conducted in the present study, further large-scale and multi-year investigations are required if a full understanding of the UAS-AgroC approach is to be achieved in relation to variations in soil hydrological properties or interannual climatic variability. While our study demonstrates the value of UAS-derived LAI for improving carbon flux estimation, several operational challenges remain in scaling this approach for large-scale agricultural management. Key considerations include balancing flight frequency, sensor limitations, and computational demands with the desired level of accuracy. Although more frequent observations would help capture finer temporal dynamics of LAI, our results suggest that at least five well-timed UAS campaigns, aligned with key phenological stages, are sufficient for reliable LAI estimation in winter wheat. This approach achieves fair carbon flux predictions ($r \geq 0.81$, RMSE$\leq$ 3.19 gC m^{-2} d^{-1}) while reducing operational costs compared to continuous monitoring.

For larger-scale applications, future efforts should focus on expanding the current AgroC-UAS framework into an AgroC-satellite monitoring system. This integrated system would combine process-based crop models with high-resolution (e.g., Sentinel-2, PlanetScope) to balance temporal resolution and spatial coverage. The resulting high-resolution carbon flux maps can directly support precision agriculture by informing data-driven fertilization and irrigation decisions at subfield scales. Future research is needed to identify optimal observation frequencies across diverse crops and landscapes, and further enhance the modelling framework by incorporating soil–vegetation interactions.

4.2. Photosynthesis approach and the contribution of LAI integration

Our study highlights notable differences in the mechanisms of the two photosynthesis approaches and demonstrates the advantage of FvCB over LUE in integrating UAS-derived LAI for GPP estimation. The original $AgroC_{FvCB}$ generally produces lower GPP estimates compared to the original $AgroC_{LUE}$ model. Furthermore, when both approaches are integrated with the same UAS-derived LAI, the $AgroC_{FvCB}$ outperforms $AgroC_{LUE}$ in GPP simulations, showing a closer match with the EC flux tower GPP measurements.

These differences and improvements can be attributed to the explicit consideration of biochemical constrains and a more accurate representation of stress responses in the FvCB approach, which accounts for acclimation mechanisms in response to CO_2 concentration and stomatal conductance. Additionally, the biochemical and physically based representation of photosynthesis in the FvCB approach, with less reliance on empirical parameter tuning, makes it more reliable for detailed coupling with RTMs (Ainsworth et al. 2007; Bambach et al., 2020; Cai et al., 2018), such as the Soil Canopy Observation, Photochemistry and Energy fluxes model (SCOPE) (van der Tol et al., 2009).

In contrast, LUE models rely on empirical relationships between light absorption and carbon fixation. The parameterization of correction factors for temperature, water stress, and other constraints is site- or PFT-specific, making it difficult for LUE models to capture seasonal GPP variability and adapt to future climate scenarios (Flanagan et al., 2015; Lin et al., 2017; Sawada and Miyachi, 1974). Additionally, these dependencies introduce uncertainties in long-term GPP estimations (Pei et al., 2022).

The improvements in GPP prediction with LAI integration stem from the established relationship between LAI and GPP, as described in Eq. (1) and Eq. (2). The overestimation of the UAS-derived LAI values in comparison to the internal developed LAI in $AgroC_{LUE}$ and $AgroC_{FvCB}$ (Fig. 3) led to higher GPP and TER estimates from June to mid-July (Fig. 4 and Fig. 5), which more closely aligned with flux tower observations. Nevertheless, GPP is not determined by LAI alone, but is also influenced by ambient light conditions, crop properties and photosynthetic mechanisms (Bayat et al., 2018; De Cannière et al., 2021; Herbst et al., 2008). This can be evident from the temporal mismatch between GPP and LAI peaks. While UAS-derived LAI reached its maximum on 26 May (Fig. 3), the GPP peaks for $AgroC_{FvCB}$ with UAS-derived LAI (Fig. 5b) and $AgroC_{LUE}$ with UAS-derived LAI (Fig. 4b) occurred later on 19 June and earlier on 28 May, respectively.

Although the integration of LAI retrieved from UAS generally improves all three carbon fluxes estimation in both $AgroC_{LUE}$ and $AgroC_{FvCB}$, its impact on TER and NEE remains relatively limited. The LAI directly relates to the shoot respiration, which contributes most to the autotrophic respiration (AR) (Suleau et al., 2011; Wang et al., 2015). However, the plant-related AR only accounts for 60 % to 80 % of total TER (Demyan et al., 2016; Suleau et al., 2011), the rest microbial HR is less influenced by LAI and remains poorly explained by plant biotic factors. Furthermore, the explicit consideration of belowground respiration processes including HR and root AR in the AgroC model also explains the general overestimation of NEE accumulation from sowing till harvest, in comparison to EC tower measurements (Table 3), as well as its tendency to produce consistently positive TER values, indicating a sustained release of CO_2 from ecosystem respiration throughout the main growing season. These findings are consistent with previous studies (Klosterhalfen et al., 2017; Schiefer et al., 2021).

Additionally, while nonlinear LAI interpolation may better capture rapid early-season growth in winter wheat crops, linear interpolation provides an assumption-free approach that aligns well with observed vegetation dynamics (Casa et al., 2012; Peng et al., 2024). Its structural simplicity makes it more suitable for scaling to large, diverse cropping systems. The use of linearly interpolated LAI to compare with or replace simulated values is also consistent with practices in existing remote sensing–driven land surface models such as SCOPE and CLM (Lawrence et al., 2019; van der Tol et al., 2009), where robustness and simplicity are prioritized for the sake of spatial integrity.

Several studies have explored modifications to the LUE approach to enhance its biochemical process representation for GPP prediction (Guan et al., 2021; H. H. Zhang et al., 2023), in which a site-level attempt to integrate FvCB into an LUE framework was achieved in the P-model (Stocker et al., 2020). However, to better account the belowground respiration processes and enhance carbon cycle predictions, including TER, further research should focus on mechanistic integration of UAS observations with biophysical processes. The coupling of the RTMs with crop growth models through biochemical FvCB photosynthesis approach could be a promising way to improve the carbon fluxes prediction in agroecosystems within the modelling framework.

5. Conclusion

In this study, we inverted the PROSAIL model against UAS imagery using a physical-based RTM inversion approach and integrated the retrieved LAI into the agroecosystem model to estimate agroecosystem carbon fluxes. Our results demonstrate that integrating UAS-derived LAI with the AgroC model improves both the temporal and spatial accuracy of agroecosystem GPP and NEE estimations, enabling high-resolution (1 m) and high-frequency (hourly) monitoring in a winter wheat field. The $AgroC_{FvCB}$ model, integrated with UAS-derived LAI, provided the most accurate daily GPP estimates, while the $AgroC_{LUE}$ model, integrated with UAS-derived LAI, delivered the best daily NEE estimates. Additionally, our approach of combining the superior performance of the $AgroC_{FvCB}$ model and the UAS-derived LAI enabled high-resolution mapping of GPP and NEE, effectively capturing within-field spatial variations in a winter wheat field.

Despite the improvements incorporating canopy physical interactions through RTM inversion and photosynthetic biochemistry through the FvCB approach, the integration of UAS-derived LAI showed limited improvement in TER estimation. This limitation is likely due to challenges in accurately capturing belowground respiration processes. These findings highlight the need to integrate UAS observations with plant biophysical processes in a more mechanistic manner. Further studies should further investigate the coupling of the RTM and AgroC models to improve the representation of agroecosystem carbon fluxes.

Overall, this study highlights the potential of integrating high-resolution UAS imagery with the AgroC model to enhance the spatio-temporal assessment of the agroecosystem carbon fluxes. Extending this approach to different crop types and environmental conditions could further validate its applicability and improve our understanding of carbon dynamics in agricultural landscapes.

CRediT authorship contribution statement

Xuerui Guo: Writing – original draft, Visualization, Validation, Software, Methodology, Investigation, Formal analysis, Data curation, Conceptualization. **Bagher Bayat:** Writing – review & editing, Supervision, Investigation, Conceptualization. **Jordan Steven Bates:** Writing – review & editing, Data curation. **Michael Herbst:** Writing – review & editing, Data curation. **Marius Schmidt:** Writing – review & editing, Data curation. **Harry Vereecken:** Writing – review & editing, Resources, Project administration, Funding acquisition, Conceptualization. **Carsten Montzka:** Writing – review & editing, Supervision, Project administration, Investigation, Conceptualization.

Declaration of competing interest

The authors declare that they have no known competing financial interests or personal relationships that could have appeared to influence the work reported in this paper.

Acknowledgements

This research was support by the Helmholtz Association Modular Observation Solutions for Earth Systems (MOSES) Initiative.

Appendix A. Supplements to the AgroC model implementation

The initial settings for $AgroC_{LUE}$ model photosynthesis parameters are listed in Table A.1. Table A.2 describes the reduction of maximum photosynthesis rate response to temperature in the LUE approach. From Table A.3, Table A.4, Table A.5, Table A.6, Table A.7 give a general view of plant growth through organ-specific dry matter partitioning and their responses to temperature.

The soil map is provided in Fig. A.1 and the corresponding properties for the majority two soil types within the study area are listed in Table A.8, Table A.9

Table A.1
Plant parameters setting for winter wheat crop relevant to LAI development and GPP simulation.

Abbreviation (Unit)	Variables	
RGR (ha/ha/ °C/d)	relative growth rate during exponential leaf area growth	0.012
SLA (ha leaf/kg DM)	Specific leaf area of new leaves	0.0016
RKDF	Extinction coefficient for diffuse PAR flux	0.75
SCP	scattering coefficient of leaves for PAR	0.2
AMX (kg CO_2/ha leaf/h)	potential CO_2 assimilation rate of a unit leaf area for light saturation	75
EFF ((kg CO_2/ha leaf/h)/(J/m2/s))	initial light use efficiency	0.5
Tempstart (°C)	Accumulate temperature for spring growth	436
NSL (N/ m^2)	number of seedlings per m^2	260

Table A.2
Daily average daytime temperature against reduction factor of the maximal light assimilation rate.

Accumulated daily temperature	Reduction factor of the maximal light assimilation rate
0.0	0.005
4.0	0.3
10.0	0.6
15.0	0.8
20.0	1.0
30.0	0.01

Table A.3
DVS against fraction of dry matter allocated to the leaves.

Development stage	Fraction of dry matter allocated to leaves
0	0.7
0.1	0.7
0.25	0.75
0.5	0.65
0.7	0.175
0.95	0
2	0

Table A.4
DVS against fraction of dry matter allocated to the shoot.

Development stage	Fraction of dry matter allocated to leaves
0	0.33
0.1	0.33
0.2	0.42
0.35	0.60
0.4	0.67
0.5	0.78
0.7	0.85
0.9	0.92
1.2	1.0
2.0	1.0

Table A.5
DVS against fraction of dry matter allocated to the stem.

Development stage	Fraction of dry matter allocated to leaves
0	0.3
0.1	0.3
0.25	0.25
0.5	0.3
0.7	0.4
0.95	0.275
1.05	0
2	0

Table A.6
Pre-anthesis reduction factor of the development rate as a function of temperature.

Accumulated daily temperature	Reduction factor of the development rate
-10	0.0000
0	0.0000
2	0.0021
5	0.0032
10	0.0064
15	0.0167
20	0.0224
25	0.0279
30	0.0335
35	0.0391
40	0.0447

Table A.7
Post-anthesis reduction factor of the development rate as a function of temperature.

Accumulated daily temperature	Reduction factor of the development rate
-10	0.0000
0	0.0000
2	0.0037
5	0.0083
10	0.0165
15	0.0157
20	0.0209
25	0.0262
30	0.0314
35	0.0367
40	0.0418

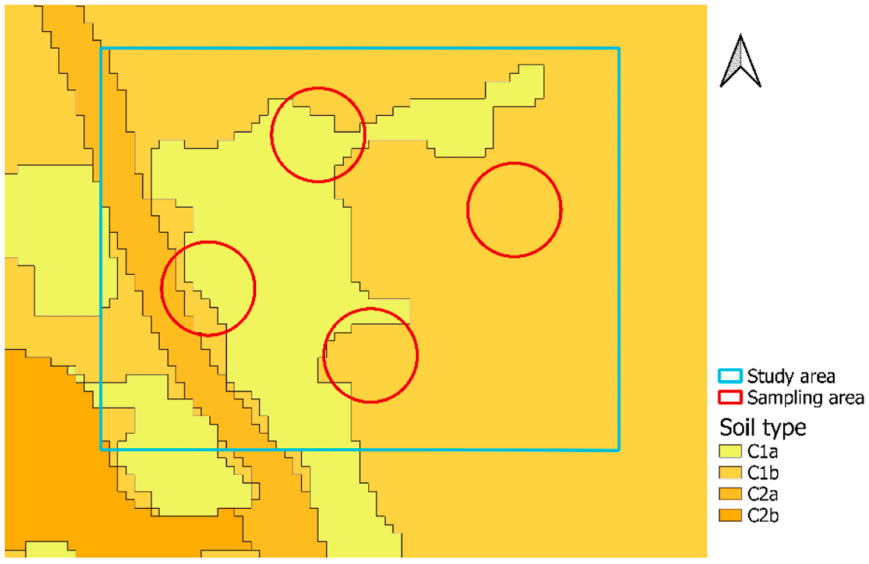

Fig. A.1. Geophysics-based soil map that provides detailed soil information of the study area gathered from (Brogi et al., 2020).

Table A.8
The averaged soil properties within the study area (Corg: organic carbon content) and calibrated hydraulic parameters (***θr***: residual water content; ***θs***: saturated water content;
α: inverse of the bubbling pressure; n: shape parameter; Ks: saturated hydraulic conductivity.

Soil type	Profile horizons	θr($cm^{-3}cm^{-3}$)	θs($cm^{-3}cm^{-3}$)	α (cm^{-1})	Ks($cm\ h^{-1}$)	n (-)
C1a	0–10 cm	0.0661	0.4405	0.0221	0.2848	1.3261
	10–30 cm	0.0659	0.4220	0.0202	0.2175	1.3253
	30–80 cm	0.0746	0.3951	0.0172	0.1287	1.3083
	80–2000 cm	0.0756	0.3937	0.0183	0.1442	1.3093
C1b	0–10 cm	0.06327	0.4444	0.0224	0.3019	1.3297
	10–30 cm	0.06309	0.4258	0.0205	0.2317	1.3293
	30–80 cm	0.07302	0.397	0.0176	0.1386	1.312
	80–2000 cm	0.07701	0.3893	0.0176	0.1287	1.3056

Table A.9
The soil properties at site. (IRPM: Initial concentration of the resistant plant material; IBIO: Initial concentration of the biomass; IHUM: Initial concentration of the humus pool; IOM: Initial concentration of the inert organic matter pool).

Soil type	Clay (%)	IRPM (g/cm-3)	IBIO (g/cm-3)	IHUM (g/cm-3)	IOM (g/cm-3)
	0.171	0.002003	0.0002486	0.0112	0.001216
	0.171	0.002003	0.0002486	0.0112	0.001216
	0.213	0.001112	0.0001463	0.006551	0.0006459
	0.110	0.001112	0.0001463	0.006551	0.0006459

Appendix B. Development stage

Fig. B.1

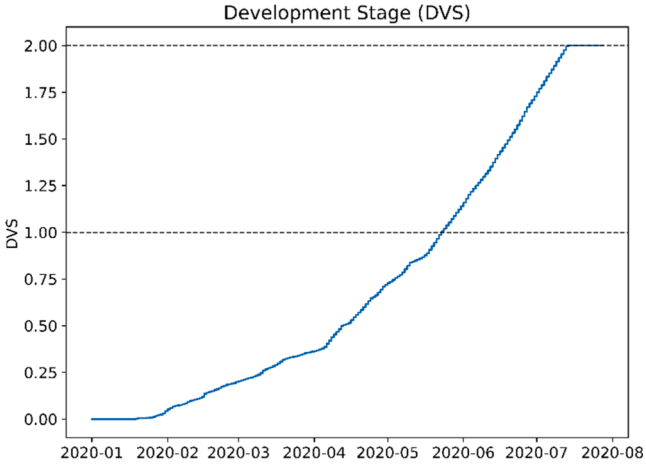

Fig. B.1. Changes in the DVS in the AgroC model. Note that the DVS depends only on temperature and is identical for all four AgroC model versions.

Appendix C. Correlation between daily observed and simulated carbon fluxes

Fig. C.1, Fig. C.2, Fig. C.3

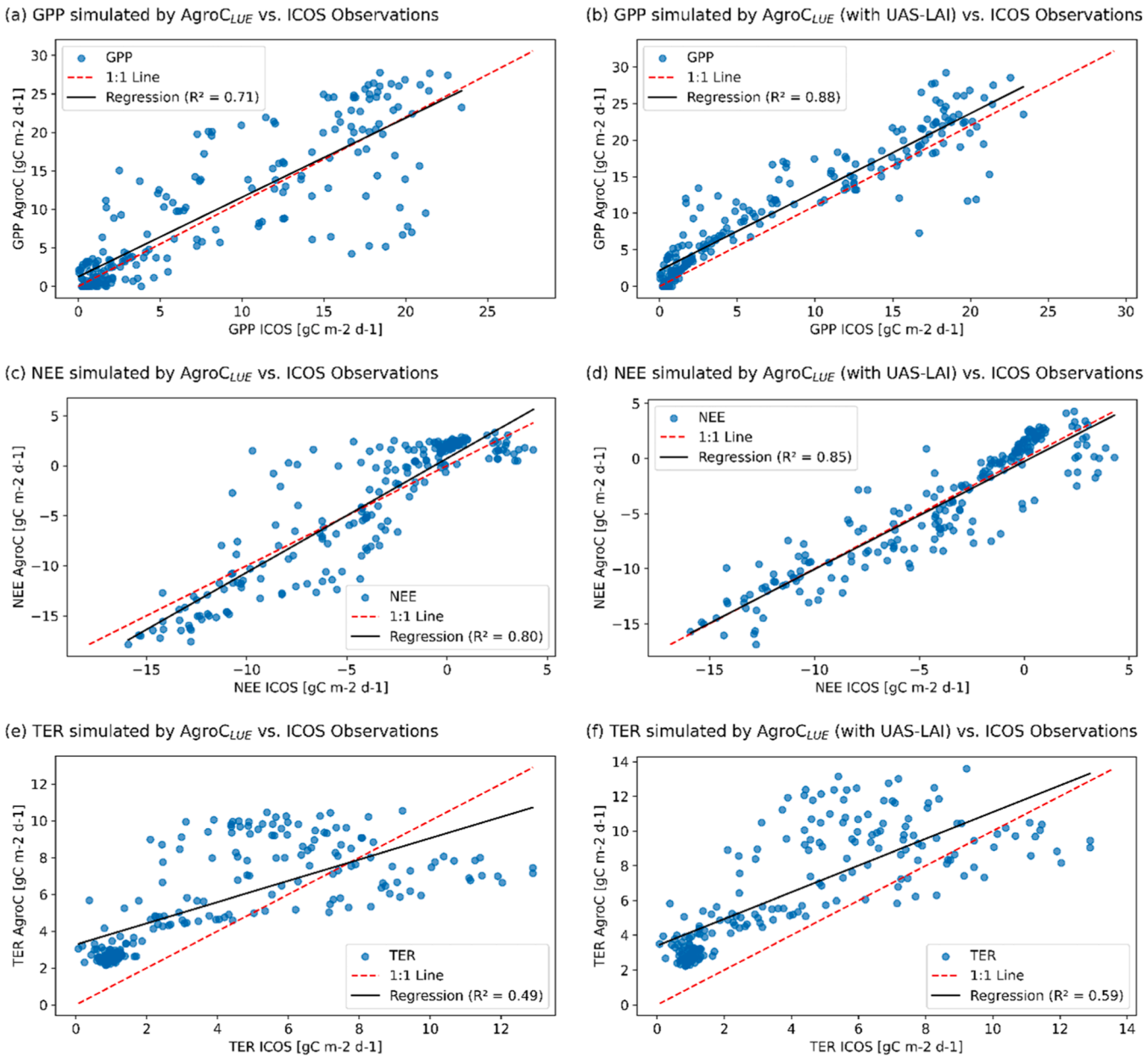

Fig. C.1. Correlation between measured and simulated daily carbon fluxes from ICOS and the AgroC$_{LUE}$ models.

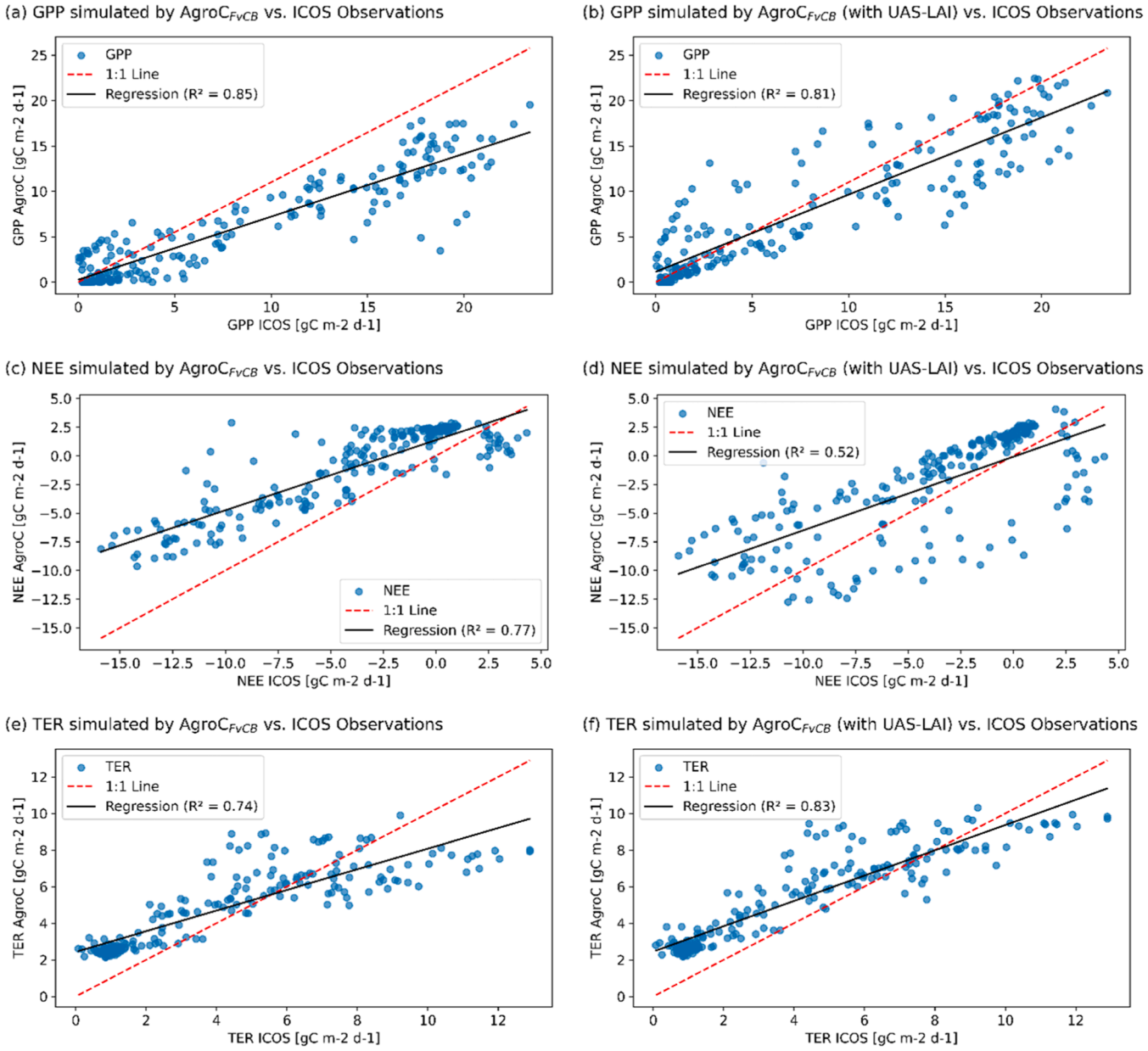

Fig. C.2. Correlation between measured and simulated daily carbon fluxes from ICOS and the AgroC$_{FvCB}$ models.

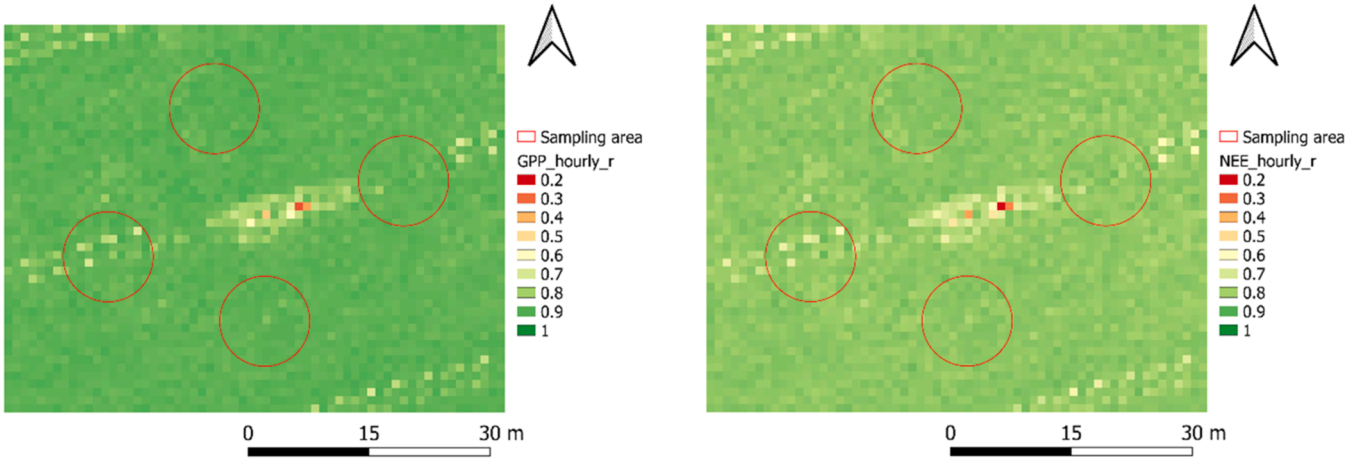

Fig. C.3. Map of Pearson correlation coefficient (***r***) for hourly GPP (left) and NEE (right) simulations over time from sowing to harvest, compared with the ICOS observations. The red circular boundaries represent the four continuous sampling plots (CPs).

Data availability

Data will be made available on request.

References

AINSWORTH, E.A., ROGERS, A., 2007. The response of photosynthesis and stomatal conductance to rising [CO $_2$]: mechanisms and environmental interactions. Plant Cell Environ. 30, 258–270. https://doi.org/10.1111/j.1365-3040.2007.01641.x.

Allen, R.G., Pereira, L.S., Raes, D., 1998. Crop evapotranspiration Guidelines for computing Crop water requirements. FAO Irrigation and Drainage Paper 56. J. Hydrol. (Amst) 5, 842.

Baldocchi, D., Falge, E., Gu, L., Olson, R., Hollinger, D., Running, S., Anthoni, P., Bernhofer, C., Davis, K., Evans, R., Fuentes, J., Goldstein, A., Katul, G., Law, B., Lee, X., Malhi, Y., Meyers, T., Munger, W., Oechel, W., Paw, K.T., Pilegaard, K., Schmid, H.P., Valentini, R., Verma, S., Vesala, T., Wilson, K., Wofsy, S., 2001. FLUXNET: A new tool to study the temporal and spatial variability of ecosystem–Scale carbon dioxide. Water Vapor, Energy Flux Densities. Bull Am Meteorol Soc 82, 2415–2434. https://doi.org/10.1175/1520-0477(2001)082<2415:FANTTS>2.3.CO;2.

Bambach, N., U, K.T.P., Gilbert, M.E., 2020. A dynamic model of RuBP-regeneration limited photosynthesis accounting for photoinhibition, heat and water stress. Agric. For. Meteorol. 285–286, 107911. https://doi.org/10.1016/j.agrformet.2020.107911.

Bates, J.S., Montzka, C., Schmidt, M., Jonard, F., 2021. Estimating canopy density parameters time-series for winter wheat using UAS mounted LiDAR. Remote Sens. (Basel) 13, 710. https://doi.org/10.3390/rs13040710.

Bayat, B., van der Tol, C., Verhoef, W., 2018. Integrating satellite optical and thermal infrared observations for improving daily ecosystem functioning estimations during a drought episode. Remote Sens. Environ. 209, 375–394. https://doi.org/10.1016/j.rse.2018.02.027.

Bayat, B., van der Tol, C., Verhoef, W., 2016. Remote sensing of grass response to drought stress using spectroscopic techniques and canopy reflectance model inversion. Remote Sens. (Basel) 8. https://doi.org/10.3390/rs8070557.

Bellucco, V., Marras, S., Grimmond, C.S.B., Järvi, L., Sirca, C., Spano, D., 2017. Modelling the biogenic CO2 exchange in urban and non-urban ecosystems through the assessment of light-response curve parameters. Agric. For. Meteorol. 236, 113–122. https://doi.org/10.1016/j.agrformet.2016.12.011.

Berger, K., Atzberger, C., Danner, M., D'Urso, G., Mauser, W., Vuolo, F., Hank, T., 2018. Evaluation of the PROSAIL model capabilities for future hyperspectral model environments: A review study. Remote Sens. (Basel) 10, 85. https://doi.org/10.3390/rs10010085.

Bernacchi, C.J., Singsaas, E.L., Pimentel, C., Portis, A.R., Long, S.P., 2001. Improved temperature response functions for models of Rubisco-limited photosynthesis. Glob. Chang. Biol. 21, 253–259. https://doi.org/10.1111/J.1365-3040.2001.00668.X.

Boas, T., Bogena, H., Grünwald, T., Heinesch, B., Ryu, D., Schmidt, M., Vereecken, H., Western, A., Franssen, H.J.H., 2021. Improving the representation of cropland sites in the Community Land Model (CLM) version 5.0. Geosci. Model. Dev. 14, 573–601. https://doi.org/10.5194/gmd-14-573-2021.

Bogena, H.R., 2016. TERENO: German network of terrestrial environmental observatories. J. Large-Scale Research Facilities JLSRF 2, A52. https://doi.org/10.17815/jlsrf-2-98.

Brilli, L., Bechini, L., Bindi, M., Carozzi, M., Cavalli, D., Conant, R., Dorich, C.D., Doro, L., Ehrhardt, F., Farina, R., Ferrise, R., Fitton, N., Francaviglia, R., Grace, P., Iocola, I., Klumpp, K., Léonard, J., Martin, R., Massad, R.S., Recous, S., Seddaiu, G., Sharp, J., Smith, P., Smith, W.N., Soussana, J.F., Bellocchi, G., 2017. Review and analysis of strengths and weaknesses of agro-ecosystem models for simulating C and N fluxes. Sci. Total Environ. 598, 445–470. https://doi.org/10.1016/j.scitotenv.2017.03.208.

Brogi, C., Huisman, J.A., Herbst, M., Weihermüller, L., Klosterhalfen, A., Montzka, C., Reichenau, T.G., Vereecken, H., 2020. Simulation of spatial variability in crop leaf area index and yield using agroecosystem modeling and geophysics-based quantitative soil information. Vadose Zone J. 19. https://doi.org/10.1002/vzj2.20009.

Brogi, C., Huisman, J.A., Weihermüller, L., Herbst, M., Vereecken, H., 2021. Added value of geophysics-based soil mapping in agro-ecosystem simulations. SOIL 7, 125–143. https://doi.org/10.5194/soil-7-125-2021.

Brown, L.A., Meier, C., Morris, H., Pastor-Guzman, J., Bai, G., Lerebourg, C., Gobron, N., Lanconelli, C., Clerici, M., Dash, J., 2020. Evaluation of global leaf area index and fraction of absorbed photosynthetically active radiation products over North America using Copernicus Ground Based Observations for Validation data. Remote Sens. Environ. 247. https://doi.org/10.1016/j.rse.2020.111935.

Bukowiecki, J., Rose, T., Holzhauser, K., Rothardt, S., Rose, M., Komainda, M., Herrmann, A., Kage, H., 2024. UAV-based canopy monitoring: calibration of a multispectral sensor for green area index and nitrogen uptake across several crops. Precis. Agric. 25, 1556–1580. https://doi.org/10.1007/s11119-024-10123-2.

Cai, C., Li, G., Yang, H., Yang, J., Liu, H., Struik, P.C., Luo, W., Yin, X., Di, L., Guo, X., Jiang, W., Si, C., Pan, G., Zhu, J., 2018. Do all leaf photosynthesis parameters of rice acclimate to elevated CO2, elevated temperature, and their combination, in FACE environments? Glob. Chang. Biol. 24, 1685–1707. https://doi.org/10.1111/gcb.13961.

Casa, R., Varella, H., Buis, S., Guérif, M., De Solan, B., Baret, F., 2012. Forcing a wheat crop model with LAI data to access agronomic variables: evaluation of the impact of model and LAI uncertainties and comparison with an empirical approach. Eur. J. Agronomy 37, 1–10. https://doi.org/10.1016/j.eja.2011.09.004.

Chakhvashvili, E., Siegmann, B., Muller, O., Verrelst, J., Bendig, J., Kraska, T., Rascher, U., 2022. Retrieval of crop variables from proximal multispectral UAV image data using PROSAIL in Maize canopy. Remote Sens. (Basel) 14. https://doi.org/10.3390/rs14051247.

Chen, Q., Zheng, B., Chenu, K., Hu, P., Chapman, S.C., 2022. Unsupervised plot-scale LAI phenotyping via UAV-based imaging, modelling, and machine learning. Plant Phenomics. https://doi.org/10.34133/2022/9768253, 2022.

Chu, H., Luo, X., Ouyang, Z., Chan, W.S., Dengel, S., Biraud, S.C., Torn, M.S., Metzger, S., Kumar, J., Arain, M.A., Arkebauer, T.J., Baldocchi, D., Bernacchi, C., Billesbach, D., Black, T.A., Blanken, P.D., Bohrer, G., Bracho, R., Brown, S., Brunsell, N.A., Chen, J., Chen, X., Clark, K., Desai, A.R., Duman, T., Durden, D., Fares, S., Forbrich, I., Gamon, J.A., Gough, C.M., Griffis, T., Helbig, M., Hollinger, D., Humphreys, E., Ikawa, H., Iwata, H., Ju, Y., Knowles, J.F., Knox, S.H., Kobayashi, H., Kolb, T., Law, B., Lee, X., Litvak, M., Liu, H., Munger, J.W., Noormets, A., Novick, K., Oberbauer, S.F., Oechel, W., Oikawa, P., Papuga, S.A., Pendall, E., Prajapati, P., Prueger, J., Quinton, W.L., Richardson, A.D., Russell, E.S., Scott, R.L., Starr, G., Staebler, R., Stoy, P.C., Stuart-Haëntjens, E., Sonnentag, O., Sullivan, R.C., Suyker, A., Ueyama, M., Vargas, R., Wood, J.D., Zona, D., 2021. Representativeness of Eddy-Covariance flux footprints for areas surrounding AmeriFlux sites. Agric. For. Meteorol. 301–302. https://doi.org/10.1016/j.agrformet.2021.108350.

Coleman, K., Jenkinson, D.S., 1996. RothC-26.3 - A model for the turnover of carbon in soil. In: Powlson, D.S., Smith, P., Smith, J.U. (Eds.), RothC-26.3 - A model for the turnover of carbon in soil. Evaluation of Soil Organic Matter Models 237–246. https://doi.org/10.1007/978-3-642-61094-3_17.

Collatz, G., Ribas-Carbo, M., Berry, J., 1992. Coupled photosynthesis-stomatal conductance model for leaves of C4 plants. Functional Plant Biol. 19, 519. https://doi.org/10.1071/PP9920519.

Danner, M., Berger, K., Wocher, M., Mauser, W., Hank, T., 2019. Fitted PROSAIL parameterization of leaf inclinations, water content and brown pigment content for winter wheat and maize canopies. Remote Sens. (Basel) 11, 1150. https://doi.org/10.3390/rs11101150.

Danner, M., Berger, K., Wocher, M., Mauser, W., Hank, T., 2017. Retrieval of biophysical crop variables from multi-angular canopy spectroscopy. Remote Sens. (Basel) 9. https://doi.org/10.3390/rs9070726.

De Cannière, S., Herbst, M., Vereecken, H., Defourny, P., Jonard, F., 2021. Constraining water limitation of photosynthesis in a crop growth model with sun-induced chlorophyll fluorescence. Remote Sens. Environ. 267. https://doi.org/10.1016/j.rse.2021.112722.

Demyan, M.S., Ingwersen, J., Funkuin, Y.N., Ali, R.S., Mirzaeitalarposhti, R., Rasche, F., Poll, C., Müller, T., Streck, T., Kandeler, E., Cadisch, G., 2016. Partitioning of ecosystem respiration in winter wheat and silage maize-modeling seasonal temperature effects. Agric. Ecosyst. Environ. 224, 131–144. https://doi.org/10.1016/j.agee.2016.03.039.

Drees, L., Demie, D.T., Paul, M.R., Leonhardt, J., Seidel, S.J., Döring, T.F., Roscher, R., 2024. Data-driven crop growth simulation on time-varying generated images using multi-conditional generative adversarial networks. Plant Methods 20. https://doi.org/10.1186/s13007-024-01205-3.

Du, D., Zheng, C., Jia, L., Chen, Q., Jiang, M., Hu, G., Lu, J., 2022. Estimation of global cropland gross primary production from satellite observations by integrating water availability variable in light-use-efficiency model. Remote Sens. (Basel) 14, 1722. https://doi.org/10.3390/rs14071722.

Duan, S.B., Li, Z.L., Wu, H., Tang, B.H., Ma, L., Zhao, E., Li, C., 2014. Inversion of the PROSAIL model to estimate leaf area index of maize, potato, and sunflower fields from unmanned aerial vehicle hyperspectral data. Int. J. Appl. Earth Obser. Geoinf. 26, 12–20. https://doi.org/10.1016/j.jag.2013.05.007.

Fang, H., Baret, F., Plummer, S., Schaepman-Strub, G., 2019a. An overview of global leaf area index (LAI): methods, products, validation, and applications. Rev. Geophys. 57, 739–799. https://doi.org/10.1029/2018RG000608.

Fang, H., Zhang, Y., Wei, S., Li, W., Ye, Y., Sun, T., Liu, W., 2019b. Validation of global moderate resolution leaf area index (LAI) products over croplands in northeastern China. Remote Sens. Environ. 233, 111377. https://doi.org/10.1016/j.rse.2019.111377.

Farquhar, G., Buckley, T., Miller, J., 2002. Optimal stomatal control in relation to leaf area and nitrogen content. Silva Fennica 36. https://doi.org/10.14214/sf.530.

Farquhar, G.D., von Caemmerer, S., Berry, J.A., 1980. A biochemical model of photosynthetic CO2 assimilation in leaves of C3 species. Planta 149, 78–90. https://doi.org/10.1007/BF00386231.

Féret, J.B., de Boissieu, F., 2024. prospect: an R package to link leaf optical properties with their chemical and structural properties with the leaf model PROSPECT. J. Open. Source Softw. 9, 6027. https://doi.org/10.21105/joss.06027.

Féret, J.B., Gitelson, A.A., Noble, S.D., Jacquemoud, S., 2017. PROSPECT-D: towards modeling leaf optical properties through a complete lifecycle. Remote Sens. Environ. 193, 204–215. https://doi.org/10.1016/j.rse.2017.03.004.

Féret, J.B., le Maire, G., Jay, S., Berveiller, D., Bendoula, R., Hmimina, G., Cheraiet, A., Oliveira, J.C., Ponzoni, F.J., Solanki, T., de Boissieu, F., Chave, J., Nouvellon, Y., Porcar-Castell, A., Proisy, C., Soudani, K., Gastellu-Etchegorry, J.P., Lefèvre-Fonollosa, M.J., 2019. Estimating leaf mass per area and equivalent water thickness based on leaf optical properties: potential and limitations of physical modeling and machine learning. Remote Sens. Environ. 231, 110959. https://doi.org/10.1016/j.rse.2018.11.002.

Flanagan, L.B., Sharp, E.J., Gamon, J.A., 2015. Application of the photosynthetic light-use efficiency model in a northern Great Plains grassland. Remote Sens. Environ. 168, 239–251. https://doi.org/10.1016/j.rse.2015.07.013.

Frank, S., Lessa Derci Augustynczik, A., Havlík, P., Boere, E., Ermolieva, T., Fricko, O., Di Fulvio, F., Gusti, M., Krisztin, T., Lauri, P., Palazzo, A., Wögerer, M., 2024. Enhanced

agricultural carbon sinks provide benefits for farmers and the climate. Nat. Food 5, 742–753. https://doi.org/10.1038/s43016-024-01039-1.
Friend, A.D., 1995. PGEN: an integrated model of leaf photosynthesis, transpiration, and conductance. Ecol. Modell. 77, 233–255. https://doi.org/10.1016/0304-3800(93)E0082-E.
García-Haro, F.J., Campos-Taberner, M., Muñoz-Marí, J., Laparra, V., Camacho, F., Sánchez-Zapero, J., Camps-Valls, G., 2018. Derivation of global vegetation biophysical parameters from EUMETSAT Polar System. ISPRS J. Photogrammetry Remote Sens. 139, 57–74. https://doi.org/10.1016/j.isprsjprs.2018.03.005.
Gielen, B., Acosta, M., Altimir, N., Buchmann, N., Cescatti, A., Ceschia, E., Fleck, S., Hörtnagl, L., Klumpp, K., Kolari, P., Lohila, A., Loustau, D., Marañon-Jimenez, S., Manise, T., Matteucci, G., Merbold, L., Metzger, C., Moureaux, C., Montagnani, L., Nilsson, M.B., Osborne, B., Papale, D., Pavelka, M., Saunders, M., Simioni, G., Soudani, K., Sonnentag, O., Tallec, T., Tuittila, E.S., Peichl, M., Pokorny, R., Vincke, C., Wohlfahrt, G., 2018. Ancillary vegetation measurements at ICOS ecosystem stations. Int. Agrophys. 32, 645–664. https://doi.org/10.1515/intag-2017-0048.
Gong, Y., Yang, K., Lin, Z., Fang, S., Wu, X., Zhu, R., Peng, Y., 2021. Remote estimation of leaf area index (LAI) with unmanned aerial vehicle (UAV) imaging for different rice cultivars throughout the entire growing season. Plant Methods 17. https://doi.org/10.1186/s13007-021-00789-4.
Guan, X., Chen, J.M., Shen, H., Xie, X., 2021. A modified two-leaf light use efficiency model for improving the simulation of GPP using a radiation scalar. Agric. For. Meteorol. 307, 108546. https://doi.org/10.1016/j.agrformet.2021.108546.
Guo, A., Ye, H., Huang, W., Qian, B., Wang, J., Lan, Y., Wang, S., 2023. Inversion of maize leaf area index from UAV hyperspectral and multispectral imagery. Comput. Electron. Agric. 212. https://doi.org/10.1016/j.compag.2023.108020.
Guo, H., Li, S., Wong, F.L., Qin, S., Wang, Y., Yang, D., Lam, H.M., 2021. Drivers of carbon flux in drip irrigation maize fields in northwest China. Carbon. Balance Manage 16. https://doi.org/10.1186/s13021-021-00176-5.
Guo, Y., Hao, F., Zhang, X., He, Y., Fu, Y.H., 2024. Improving maize yield estimation by assimilating UAV-based LAI into WOFOST model. Field. Crops. Res. 315. https://doi.org/10.1016/j.fcr.2024.109477.
Gupta, H.V., Kling, H., Yilmaz, K.K., Martinez, G.F., 2009. Decomposition of the mean squared error and NSE performance criteria: implications for improving hydrological modelling. J. Hydrol. (Amst) 377, 80–91. https://doi.org/10.1016/j.jhydrol.2009.08.003.
Herbst, M., Hellebrand, H.J., Bauer, J., Huisman, J.A., Šimůnek, J., Weihermüller, L., Graf, A., Vanderborght, J., Vereecken, H., 2008. Multiyear heterotrophic soil respiration: evaluation of a coupled CO2 transport and carbon turnover model. Ecol. Modell. 214, 271–283. https://doi.org/10.1016/j.ecolmodel.2008.02.007.
Herbst, M., Pohlig, P., Graf, A., Weihermüller, L., Schmidt, M., Vanderborght, J., Vereecken, H., 2021. Quantification of water stress induced within-field variability of carbon dioxide fluxes in a sugar beet stand. Agric. For. Meteorol. 297, 108242. https://doi.org/10.1016/j.agrformet.2020.108242.
Huang, J., Ma, H., Sedano, F., Lewis, P., Liang, S., Wu, Q., Su, W., Zhang, X., Zhu, D., 2019. Evaluation of regional estimates of winter wheat yield by assimilating three remotely sensed reflectance datasets into the coupled WOFOST–PROSAIL model. Eur. J. Agronomy 102, 1–13. https://doi.org/10.1016/j.eja.2018.10.008.
ICOS, R.I., 2023. Ecosystem final quality (L2) product in ETC-archive format - release 2023-1 (Version 1.0). https://doi.org/10.18160/YDH2-VFYE.
Jacquemoud, S., Baret, F., 1990. PROSPECT: A model of leaf optical properties spectra. Remote Sens. Environ. 34, 75–91. https://doi.org/10.1016/0034-4257(90)90100-Z.
Jiang, S., Zhao, L., Liang, C., Cui, N., Gong, D., Wang, Y., Feng, Y., Hu, X., Zou, Q., 2021. Comparison of satellite-based models for estimating gross primary productivity in agroecosystems. Agric. For. Meteorol. 297. https://doi.org/10.1016/j.agrformet.2020.108253.
Jin, Z., Liu, H., Cao, H., Li, S., Yu, F., Xu, T., 2025. Hyperspectral remote sensing estimation of rice canopy LAI and LCC by UAV coupled RTM and machine learning. Agriculture (Switzerland) 15. https://doi.org/10.3390/agriculture15010011.
Khodjaev, S., Kuhn, L., Bobojonov, I., Glauben, T., 2024. Combining multiple UAV-based indicators for wheat yield estimation, a case study from Germany. Eur. J. Remote Sens. 57. https://doi.org/10.1080/22797254.2023.2294121.
Klosterhalfen, A., Herbst, M., Weihermüller, L., Graf, A., Schmidt, M., Stadler, A., Schneider, K., Subke, J.A., Huisman, J.A., Vereecken, H., 2017. Multi-site calibration and validation of a net ecosystem carbon exchange model for croplands. Ecol. Modell. 363, 137–156. https://doi.org/10.1016/j.ecolmodel.2017.07.028.
Kong, W., Huang, W., Zhou, X., Song, X., Casa, R., 2016. Estimation of carotenoid content at the canopy scale using the carotenoid triangle ratio index from in situ and simulated hyperspectral data. J. Appl. Remote Sens. 10, 026035. https://doi.org/10.1117/1.jrs.10.026035.
Krause, A., Papastefanou, P., Gregor, K., Layritz, L.S., Zang, C.S., Buras, A., Li, X., Xiao, J., Rammig, A., 2022. Quantifying the impacts of land cover change on gross primary productivity globally. Sci. Rep. 12. https://doi.org/10.1038/s41598-022-23120-0.
Lal, R., 2004. Soil carbon sequestration impacts on global climate change and food security. Science (1979) 304, 1623–1627. https://doi.org/10.1126/science.1097396 (1979).
Lawrence, D.M., Fisher, R.A., Koven, C.D., Oleson, K.W., Swenson, S.C., Bonan, G., Collier, N., Ghimire, B., van Kampenhout, L., Kennedy, D., Kluzek, E., Lawrence, P.J., Li, F., Li, H., Lombardozzi, D., Riley, W.J., Sacks, W.J., Shi, M., Vertenstein, M., Wieder, W.R., Xu, C., Ali, A.A., Badger, A.M., Bisht, G., van den Broeke, M., Brunke, M.A., Burns, S.P., Buzan, J., Clark, M., Craig, A., Dahlin, K., Drewniak, B., Fisher, J.B., Flanner, M., Fox, A.M., Gentine, P., Hoffman, F., Keppel-Aleks, G., Knox, R., Kumar, S., Lenaerts, J., Leung, L.R., Lipscomb, W.H., Lu, Y., Pandey, A., Pelletier, J.D., Perket, J., Randerson, J.T., Ricciuto, D.M., Sanderson, B.M., Slater, A., Subin, Z.M., Tang, J., Thomas, R.Q., Val Martin, M., Zeng, X., 2019. The community land model version 5: description of new features, benchmarking, and impact of forcing uncertainty. J. Adv. Model. Earth. Syst. 11, 4245–4287. https://doi.org/10.1029/2018MS001583.
Li, H., Yan, X., Su, P., Su, Y., Li, J., Xu, Z., Gao, C., Zhao, Y., Feng, M., Shafiq, F., Xiao, L., Yang, W., Qiao, X., Wang, C., 2025. Estimation of winter wheat <scp>LAI</scp>based on color indices and texture features of <scp>RGB</scp>images taken by <scp>UAV</scp>. J. Sci. Food Agric. 105, 189–200. https://doi.org/10.1002/jsfa.13817.
Li, W., Weiss, M., Waldner, F., Defourny, P., Demarez, V., Morin, D., Hagolle, O., Baret, F., 2015. A generic algorithm to estimate LAI, FAPAR and FCOVER variables from SPOT4_HRVIR and landsat sensors: evaluation of the consistency and comparison with ground measurements. Remote Sens. (Basel) 7, 15494–15516. https://doi.org/10.3390/rs71115494.
Lian, Y., Li, H., Renyang, Q., Liu, L., Dong, J., Liu, X., Qu, Z., Lee, L.C., Chen, L., Wang, D., Zhang, H., 2023. Mapping the net ecosystem exchange of CO2 of global terrestrial systems. Int. J. Appl. Earth Observ. Geoinf. 116, 103176. https://doi.org/10.1016/j.jag.2022.103176.
Lin, X., Chen, B., Chen, J., Zhang, H., Sun, S., Xu, G., Guo, L., Ge, M., Qu, J., Li, L., Kong, Y., 2017. Seasonal fluctuations of photosynthetic parameters for light use efficiency models and the impacts on gross primary production estimation. Agric. For. Meteorol. 236, 22–35. https://doi.org/10.1016/J.AGRFORMET.2016.12.019.
Liu, L., Zhou, W., Guan, K., Peng, B., Xu, S., Tang, J., Zhu, Q., Till, J., Jia, X., Jiang, C., Wang, S., Qin, Z., Kong, H., Grant, R., Mezbahuddin, S., Kumar, V., Jin, Z., 2024. Knowledge-guided machine learning can improve carbon cycle quantification in agroecosystems. Nat. Commun. 15. https://doi.org/10.1038/s41467-023-43860-5.
Liu, Y., Xiao, J., Ju, W., Zhu, G., Wu, X., Fan, W., Li, D., Zhou, Y., 2018. Satellite-derived LAI products exhibit large discrepancies and can lead to substantial uncertainty in simulated carbon and water fluxes. Remote Sens. Environ. 206, 174–188. https://doi.org/10.1016/j.rse.2017.12.024.
Meiyan, S., Mengyuan, S., Qizhou, D., Xiaohong, Y., Baoguo, L., Yuntao, M., 2022. Estimating the maize above-ground biomass by constructing the tridimensional concept model based on UAV-based digital and multi-spectral images. Field. Crops. Res. 282. https://doi.org/10.1016/j.fcr.2022.108491.
Meroni, M., Fasbender, D., Lopez-Lozano, R., Migliavacca, M., 2019. Assimilation of earth observation data over cropland and grassland sites into a simple GPP model. Remote Sens. (Basel) 11. https://doi.org/10.3390/rs11070749.
MicaSense, 2017. MicaSense RedEdge-M™ multispectral camera user manual.
Noh, N.J., Renchon, A.A., Knauer, J., Haverd, V., Li, J., Griebel, A., Barton, C.V.M., Yang, J., Sihi, D., Arndt, S.K., Davidson, E.A., Tjoelker, M.G., Pendall, E., 2024. Reconciling top-down and bottom-up estimates of ecosystem respiration in a mature eucalypt forest. J. Geophys. Res. Biogeosci. 129. https://doi.org/10.1029/2024JG008064.
Nordbo, A., Järvi, L., Haapanala, S., Wood, C.R., Vesala, T., 2012. Fraction of natural area as main predictor of net CO2 emissions from cities. Geophys. Res. Lett. 39. https://doi.org/10.1029/2012GL053087.
Pacheco-Labrador, J., Migliavacca, M., Ma, X., Mahecha, M., Carvalhais, N., Weber, U., Benavides, R., Bouriaud, O., Barnoaiea, I., Coomes, D.A., Bohn, F.J., Kraemer, G., Heiden, U., Huth, A., Wirth, C., 2022. Challenging the link between functional and spectral diversity with radiative transfer modeling and data. Remote Sens. Environ. 280. https://doi.org/10.1016/j.rse.2022.113170.
Pastorello, G., Trotta, C., Canfora, E., Chu, H., Christianson, D., Cheah, Y.W., Poindexter, C., Chen, J., Elbashandy, A., Humphrey, M., Isaac, P., Polidori, D., Reichstein, M., Ribeca, A., van Ingen, C., Vuichard, N., Zhang, L., Amiro, B., Ammann, C., Arain, M.A., Ardö, J., Arkebauer, T., Arndt, S.K., Arriga, N., Aubinet, M., Aurela, M., Baldocchi, D., Barr, A., Beamesderfer, E., Marchesini, L.B., Bergeron, O., Beringer, J., Bernhofer, C., Berveiller, D., Billesbach, D., Black, T.A., Blanken, P.D., Bohrer, G., Boike, J., Bolstad, P.V., Bonal, D., Bonnefond, J.M., Bowling, D.R., Bracho, R., Brodeur, J., Brümmer, C., Buchmann, N., Burban, B., Burns, S.P., Buysse, P., Cale, P., Cavagna, M., Cellier, P., Chen, S., Chini, I., Christensen, T.R., Cleverly, J., Collalti, A., Consalvo, C., Cook, B.D., Cook, D., Coursolle, C., Cremonese, E., Curtis, P.S., D'Andrea, E., da Rocha, H., Dai, X., Davis, K.J., Cinti, B.De, Grandcourt, A.de, Ligne, A.De, De Oliveira, R.C., Delpierre, N., Desai, A.R., Di Bella, C.M., Tommasi, P.di, Dolman, H., Domingo, F., Dong, G., Dore, S., Duce, P., Dufrêne, E., Dunn, A., Dušek, J., Eamus, D., Eichelmann, U., ElKhidir, H.A.M., Eugster, W., Ewenz, C.M., Ewers, B., Famulari, D., Fares, S., Feigenwinter, I., Feitz, A., Fensholt, R., Filippa, G., Fischer, M., Frank, J., Galvagno, M., Gharun, M., Gianelle, D., Gielen, B., Gioli, B., Gitelson, A., Goded, I., Goeckede, M., Goldstein, A.H., Gough, C.M., Goulden, M.L., Graf, A., Griebel, A., Gruening, C., Grünwald, T., Hammerle, A., Han, S., Han, X., Hansen, B.U., Hanson, C., Hatakka, J., He, Y., Hehn, M., Heinesch, B., Hinko-Najera, N., Hörtnagl, L., Hutley, L., Ibrom, A., Ikawa, H., Jackowicz-Korczynski, M., Janouš, D., Jans, W., Jassal, R., Jiang, S., Kato, T., Khomik, M., Klatt, J., Knohl, A., Knox, S., Kobayashi, H., Koerber, G., Kolle, O., Kosugi, Y., Kotani, A., Kowalski, A., Kruijt, B., Kurbatova, J., Kutsch, W.L., Kwon, H., Launiainen, S., Laurila, T., Law, B., Leuning, R., Li, Yingnian, Liddell, M., Limousin, J.M., Lion, M., Liska, A.J., Lohila, A., López-Ballesteros, A., López-Blanco, E., Loubet, B., Loustau, D., Lucas-Moffat, A., Lüers, J., Ma, S., Macfarlane, C., Magliulo, V., Maier, R., Mammarella, I., Manca, G., Marcolla, B., Margolis, H.A., Marras, S., Massman, W., Mastepanov, M., Matamala, R., Matthes, J.H., Mazzenga, F., McCaughey, H., McHugh, I., McMillan, A.M.S., Merbold, L., Meyer, W., Meyers, T., Miller, S.D., Minerbi, S., Moderow, U., Monson, R.K., Montagnani, L., Moore, C.E., Moors, E., Moreaux, V., Moureaux, C., Munger, J.W., Nakai, T., Neirynck, J., Nesic, Z., Nicolini, G., Noormets, A., Northwood, M., Nosetto, M., Nouvellon, Y., Novick, K., Oechel, W., Olesen, J.E., Ourcival, J.M., Papuga, S.A., Parmentier, F.J., Paul-Limoges, E., Pavelka, M., Peichl, M., Pendall, E., Phillips, R.P., Pilegaard, K., Pirk, N., Posse, G.,

Powell, T., Prasse, H., Prober, S.M., Rambal, S., Rannik, Ü., Raz-Yaseef, N., Rebmann, C., Reed, D., Dios, V.R.de, Restrepo-Coupe, N., Reverter, B.R., Roland, M., Sabbatini, S., Sachs, T., Saleska, S.R., Sánchez-Cañete, E.P., Sanchez-Mejia, Z.M., Schmid, H.P., Schmidt, M., Schneider, K., Schrader, F., Schroder, I., Scott, R.L., Sedlák, P., Serrano-Ortíz, P., Shao, C., Shi, P., Shironya, I., Siebicke, L., Šigut, L., Silberstein, R., Sirca, C., Spano, D., Steinbrecher, R., Stevens, R.M., Sturtevant, C., Suyker, A., Tagesson, T., Takanashi, S., Tang, Y., Tapper, N., Thom, J., Tomassucci, M., Tuovinen, J.P., Urbanski, S., Valentini, R., van der Molen, M., van Gorsel, E., van Huissteden, K., Varlagin, A., Verfaillie, J., Vesala, T., Vincke, C., Vitale, D., Vygodskaya, N., Walker, J.P., Walter-Shea, E., Wang, H., Weber, R., Westermann, S., Wille, C., Wofsy, S., Wohlfahrt, G., Wolf, S., Woodgate, W., Li, Yuelin, Zampedri, R., Zhang, J., Zhou, G., Zona, D., Agarwal, D., Biraud, S., Torn, M., Papale, D., 2020. The FLUXNET2015 dataset and the ONEFlux processing pipeline for eddy covariance data. Sci. Data 7, 225. https://doi.org/10.1038/s41597-020-0534-3.

Paustian, K., Collier, S., Baldock, J., Burgess, R., Creque, J., DeLonge, M., Dungait, J., Ellert, B., Frank, S., Goddard, T., Govaerts, B., Grundy, M., Henning, M., Izaurralde, R.C., Madaras, M., McConkey, B., Porzig, E., Rice, C., Searle, R., Seavy, N., Skalsky, R., Mulhern, W., Jahn, M., 2019. Quantifying carbon for agricultural soil management: from the current status toward a global soil information system. Carbon. Manage. https://doi.org/10.1080/17583004.2019.1633231.

Pei, Y., Dong, J., Zhang, Y., Yuan, W., Doughty, R., Yang, J., Zhou, D., Zhang, L., Xiao, X., 2022. Evolution of light use efficiency models: improvement, uncertainties, and implications. Agric. For. Meteorol. https://doi.org/10.1016/j.agrformet.2022.108905.

Peng, R., Yan, K., Liu, J., Gao, S., Pu, J., Maeda, E.E., Zhu, P., Knyazikhin, Y., Myneni, R. B., 2024. Revisiting the consistency of MODIS LAI products from a new perspective of spatiotemporal variability. Int. J. Digit. Earth. 17. https://doi.org/10.1080/17538947.2024.2407045.

Peng, X., Han, W., Ao, J., Wang, Y., 2021. Assimilation of LAI derived from UAV multispectral data into the SAFY model to estimate maize yield. Remote Sens. (Basel) 13, 1094. https://doi.org/10.3390/rs13061094.

PIX4Dmapper, 2017. PIX4Dmapper-Offline Getting Started and Manual. Lausanne, Switzerland.

Post, H., Vrugt, J.A., Fox, A., Vereecken, H., Hendricks Franssen, H.J., 2017. Estimation of Community Land Model parameters for an improved assessment of net carbon fluxes at European sites. J. Geophys. Res. Biogeosci. 122, 661–689. https://doi.org/10.1002/2015JG003297.

Putkiranta, P., Räsänen, A., Korpelainen, P., Erlandsson, R., Kolari, T.H.M., Pang, Y., Villoslada, M., Wolff, F., Kumpula, T., Virtanen, T., 2024. The value of hyperspectral UAV imagery in characterizing tundra vegetation. Remote Sens. Environ. 308, 114175. https://doi.org/10.1016/j.rse.2024.114175.

Rebmann, C., Aubinet, M., Schmid, H., Arriga, N., Aurela, M., Burba, G., Clement, R., De Ligne, A., Fratini, G., Gielen, B., Grace, J., Graf, A., Gross, P., Haapanala, S., Herbst, M., Hörtnagl, L., Ibrom, A., Joly, L., Kljun, N., Kolle, O., Kowalski, A., Lindroth, A., Loustau, D., Mammarella, I., Mauder, M., Merbold, L., Metzger, S., Mölder, M., Montagnani, L., Papale, D., Pavelka, M., Peichl, M., Roland, M., Serrano-Ortiz, P., Siebicke, L., Steinbrecher, R., Tuovinen, J.P., Vesala, T., Wohlfahrt, G., Franz, D., 2018. ICOS eddy covariance flux-station site setup: a review. Int. Agrophys. 32, 471–494. https://doi.org/10.1515/intag-2017-0044.

Revill, A., Emmel, C., D'Odorico, P., Buchmann, N., Hörtnagl, L., Eugster, W., 2019. Estimating cropland carbon fluxes: A process-based model evaluation at a Swiss crop-rotation site. Field. Crops. Res. 234, 95–106. https://doi.org/10.1016/j.fcr.2019.02.006.

Sawada, S.I., Miyachi, S., 1974. Effects of growth temperture on photosynthetic carbon metabolism in green plants I. Photosynthetic activites of various plants acclimatized to varied temperatures. Plant Cell Physiol. 15, 111–120. https://doi.org/10.1093/oxfordjournals.pcp.a074970.

Schiefer, F., Schmidtlein, S., Kattenborn, T., 2021. The retrieval of plant functional traits from canopy spectra through RTM-inversions and statistical models are both critically affected by plant phenology. Ecol. Indic. 121. https://doi.org/10.1016/j.ecolind.2020.107062.

Schmidt, M., Bagheri, S., Becker, N., Dolfus, D., Esser, O., Graf, A., Haustein, A., Kettler, M., Kummer, S., Mattes, J., 2025. ETC L2 ARCHIVE from Selhausen Juelich, 2019–2024.

Shirkey, G., John, R., Chen, J., Dahlin, K., Abraha, M., Sciusco, P., Lei, C., Reed, D.E., 2022. Fine resolution remote sensing spectra improves estimates of gross primary production of croplands. Agric. For. Meteorol. 326, 109175. https://doi.org/10.1016/j.agrformet.2022.109175.

Šimůnek, J., Suarez, D.L., 1993. Modeling of carbon dioxide transport and production in soil: 1. model development. Water. Resour. Res. 29, 487–497. https://doi.org/10.1029/92WR02225.

Smith, P., Smith, J.U., Powlson, D.S., McGill, W.B., Arah, J.R.M., Chertov, O.G., Coleman, K., Franko, U., Frolking, S., Jenkinson, D.S., Jensen, L.S., Kelly, R.H., Klein-Gunnewiek, H., Komarov, A.S., Li, C., Molina, J.A.E., Mueller, T., Parton, W.J., Thornley, J.H.M., Whitmore, A.P., 1997. A comparison of the performance of nine soil organic matter models using datasets from seven long-term experiments. Geoderma 81, 153–225. https://doi.org/10.1016/S0016-7061(97)00087-6.

Spitters, C.J.T., van Keulen, H., van Kraalingen, D.W.G., 1989. A simple and universal crop growth simulator: SUCROS87. In: Rabbinge, R., Ward, S.A., van Laar, H.H. (Eds.), Simulation and Systems Management in Crop Protection. Simulation Monographs. Pudoc, Wageningen, pp. 147–181.

Stocker, B.D., Wang, H., Smith, N.G., Harrison, S.P., Keenan, T.F., Sandoval, D., Davis, T., Prentice, I.C., 2020. P-model v1.0: an optimality-based light use efficiency model for simulating ecosystem gross primary production. Geosci. Model. Dev. 13, 1545–1581. https://doi.org/10.5194/gmd-13-1545-2020.

Storm, I., Karstens, U., D'Onofrio, C., Vermeulen, A., Peters, W., 2023. A view of the European carbon flux landscape through the lens of the ICOS atmospheric observation network. Atmos. Chem. Phys. 23, 4993–5008. https://doi.org/10.5194/acp-23-4993-2023.

Suleau, M., Moureaux, C., Dufranne, D., Buysse, P., Bodson, B., Destain, J.P., Heinesch, B., Debacq, A., Aubinet, M., 2011. Respiration of three Belgian crops: partitioning of total ecosystem respiration in its heterotrophic, above- and below-ground autotrophic components. Agric. For. Meteorol. 151, 633–643. https://doi.org/10.1016/j.agrformet.2011.01.012.

Sulis, M., Langensiepen, M., Shrestha, P., Schickling, A., Simmer, C., Kollet, S.J., 2015. Evaluating the influence of plant-specific physiological parameterizations on the partitioning of land surface energy fluxes. J. Hydrometeorol. 16, 517–533. https://doi.org/10.1175/JHM-D-14-0153.1.

Sun, B., Wang, C., Yang, C., Xu, B., Zhou, G., Li, X., Xie, J., Xu, S., Liu, B., Xie, T., Kuai, J., Zhang, J., 2021. Retrieval of rapeseed leaf area index using the PROSAIL model with canopy coverage derived from UAV images as a correction parameter. Int. J. Appl. Earth Obser. Geoinf. 102, 102373. https://doi.org/10.1016/j.jag.2021.102373.

Sun, W., Luo, X., Fang, Y., Shiga, Y.P., Zhang, Y., Fisher, J.B., Keenan, T.F., Michalak, A. M., 2023. Biome-scale temperature sensitivity of ecosystem respiration revealed by atmospheric CO2 observations. Nat. Ecol. Evol. 7, 1199–1210. https://doi.org/10.1038/s41559-023-02093-x.

Tang, Y., Zhou, R., He, P., Yu, M., Zheng, H., Yao, X., Cheng, T., Zhu, Y., Cao, W., Tian, Y., 2023. Estimating wheat grain yield by assimilating phenology and LAI with the WheatGrow model based on theoretical uncertainty of remotely sensed observation. Agric. For. Meteorol. 339, 109574. https://doi.org/10.1016/j.agrformet.2023.109574.

Tao, H., Feng, H., Xu, L., Miao, M., Long, H., Yue, J., Li, Z., Yang, G., Yang, X., Fan, L., 2020. Estimation of crop growth parameters using UAV-based hyperspectral remote sensing data. Sensors 20, 1296. https://doi.org/10.3390/s20051296.

van der Tol, C., Verhoef, W., Timmermans, J., Verhoef, A., Su, Z., 2009. An integrated model of soil-canopy spectral radiances, photosynthesis, fluorescence, temperature and energy balance. Biogeosciences. 6, 3109–3129. https://doi.org/10.5194/bg-6-3109-2009.

Van Dijke, A.J.H., Mallick, K., Schlerf, M., MacHwitz, M., Herold, M., Teuling, A.J., 2020. Examining the link between vegetation leaf area and land-atmosphere exchange of water, energy, and carbon fluxes using FLUXNET data. Biogeosciences. 17, 4443–4457. https://doi.org/10.5194/bg-17-4443-2020.

Van Laar, H.H., Goudriaan, J., Van Keulen, H., 1997. SUCROS97: Simulation of Crop Growth for Potential and Water-Limited Production situations. as applied to Spring Wheat. AB-DLO, Wageningen/Haren.

Verger, A., Vigneau, N., Chéron, C., Gilliot, J.M., Comar, A., Baret, F., 2014. Green area index from an unmanned aerial system over wheat and rapeseed crops. Remote Sens. Environ. 152, 654–664. https://doi.org/10.1016/j.rse.2014.06.006.

Verhoef, W., 1998. Theory of Radiative Transfer Models Applied in Optical Remote Sensing of Vegetation canopies : E-Book. Landbouwuniversiteit Wageningen (LUW), Wageningen.

Verhoef, W., 1984. Light scattering by leaf layers with application to canopy reflectance modeling: the SAIL model. Remote Sens. Environ. 16, 125–141. https://doi.org/10.1016/0034-4257(84)90057-9.

Verhoef, W., Jia, L., Xiao, Q., Su, Z., 2007. Unified optical-thermal four-stream radiative transfer theory for homogeneous vegetation canopies. IEEE Trans. Geosci. Remote Sens. 45, 1808–1822. https://doi.org/10.1109/TGRS.2007.895844.

Vigneault, P., Lafond-Lapalme, J., Deshaies, A., Khun, K., de la Sablonnière, S., Filion, M., Longchamps, L., Mimee, B., 2024. An integrated data-driven approach to monitor and estimate plant-scale growth using UAV. ISPRS Open J. Photogrammetry Remote Sens. 11, 100052. https://doi.org/10.1016/j.ophoto.2023.100052.

Wang, X., Ma, M., Li, X., Song, Y., Tan, J., Huang, G., Zhang, Z., Zhao, T., Feng, J., Ma, Z., Wei, W., Bai, Y., 2013. Validation of MODIS-GPP product at 10 flux sites in northern China. Int. J. Remote Sens. 34, 587–599. https://doi.org/10.1080/01431161.2012.715774.

Wang, Y., Hu, C., Dong, W., Li, X., Zhang, Y., Qin, S., Oenema, O., 2015. Carbon budget of a winter-wheat and summer-maize rotation cropland in the North China plain. Agric. Ecosyst. Environ. 206, 33–45. https://doi.org/10.1016/j.agee.2015.03.016.

Weiss, M., Baret, F., Jay, S., 2020. S2ToolBox Level 2 products: LAI, FAPAR, FCOVER Version 2.0. Avignon, France.

Wolanin, A., Camps-Valls, G., Gómez-Chova, L., Mateo-García, G., van der Tol, C., Zhang, Y., Guanter, L., 2019. Estimating crop primary productivity with Sentinel-2 and Landsat 8 using machine learning methods trained with radiative transfer simulations. Remote Sens. Environ. 225, 441–457. https://doi.org/10.1016/j.rse.2019.03.002.

Xiao, J., Chevallier, F., Gomez, C., Guanter, L., Hicke, J.A., Huete, A.R., Ichii, K., Ni, W., Pang, Y., Rahman, A.F., Sun, G., Yuan, W., Zhang, L., Zhang, X., 2019. Remote sensing of the terrestrial carbon cycle: A review of advances over 50 years. Remote Sens. Environ. 233, 111383. https://doi.org/10.1016/j.rse.2019.111383.

Yan, K., Park, T., Chen, C., Xu, B., Song, W., Yang, B., Zeng, Y., Liu, Z., Yan, G., Knyazikhin, Y., Myneni, R.B., 2018. Generating global products of LAI and FPAR from SNPP-VIIRS data: theoretical background and implementation. IEEE Trans. Geosci. Remote Sens. 56, 2119–2137. https://doi.org/10.1109/TGRS.2017.2775247.

Yang, N., Zhang, Z., Zhang, J., Guo, Y., Yang, X., Yu, G., Bai, X., Chen, J., Chen, Y., Shi, L., Li, X., 2023. Improving estimation of maize leaf area index by combining of UAV-based multispectral and thermal infrared data: the potential of new texture index. Comput. Electron. Agric. 214, 108294. https://doi.org/10.1016/j.compag.2023.108294.

Yu, F.H., Xu, T.Y., Du, W., Ma, H., Zhang, G.S., Chen, C.L., 2017. Radiative transfer models (RTMs) for field phenotyping inversion of rice based on UAV hyperspectral remote sensing. Int. J. Agricult. Biol. Eng. 10, 150–157. https://doi.org/10.25165/j.ijabe.20171004.3076.

Yuan, W., Liu, S., Yu, G., Bonnefond, J.M., Chen, J., Davis, K., Desai, A.R., Goldstein, A. H., Gianelle, D., Rossi, F., Suyker, A.E., Verma, S.B., 2010. Global estimates of evapotranspiration and gross primary production based on MODIS and global meteorology data. Remote Sens. Environ. 114, 1416–1431. https://doi.org/10.1016/j.rse.2010.01.022.

Yue, Z., Li, Zhao, Yu, G., Chen, Z., Shi, P., Qiao, Y., Du, K., Tian, C., Zhao, F.H., Leng, P., Li, Zhaoxin, Cheng, H., Chen, G., Li, F., 2023. Seasonal variations and driving mechanisms of CO2 fluxes over a winter-wheat and summer-maize rotation cropland in the North China plain. Agric. For. Meteorol. 342. https://doi.org/10.1016/j.agrformet.2023.109699.

Zhang, H., Bai, J., Sun, R., Wang, Y., Xiao, Z., Song, B., 2023. An improved light use efficiency model by considering canopy nitrogen concentrations and multiple environmental factors. Agric. For. Meteorol. 332, 109359. https://doi.org/10.1016/j.agrformet.2023.109359.

Zhang, Y., Xiao, X., Wu, X., Zhou, S., Zhang, G., Qin, Y., Dong, J., 2017. A global moderate resolution dataset of gross primary production of vegetation for 2000-2016. Sci. Data 4, 170165. https://doi.org/10.1038/sdata.2017.165.

Zhou, W., Guan, K., Peng, B., Tang, J., Jin, Z., Jiang, C., Grant, R., Mezbahuddin, S., 2021. Quantifying carbon budget, crop yields and their responses to environmental variability using the ecosys model for U.S. Midwestern agroecosystems. Agric. For. Meteorol. 307, 108521. https://doi.org/10.1016/j.agrformet.2021.108521.

Zhou, X., Zheng, H.B., Xu, X.Q., He, J.Y., Ge, X.K., Yao, X., Cheng, T., Zhu, Y., Cao, W.X., Tian, Y.C., 2017. Predicting grain yield in rice using multi-temporal vegetation indices from UAV-based multispectral and digital imagery. ISPRS J. Photogrammetry Remote Sens. 130, 246–255. https://doi.org/10.1016/j.isprsjprs.2017.05.003.